

Relaxation and noise-driven oscillations in a model of mitotic spindle dynamics

Dionn Hargreaves^{1*}, Sarah Woolner¹ and Oliver E. Jensen²

^{1*}Faculty of Biology, Medicine and Health, University of Manchester,
Oxford Road, Manchester, M13 9PL, UK.

²Department of Mathematics, University of Manchester, Oxford Road,
Manchester, M13 9PL, UK.

*Corresponding author(s). E-mail(s):

dionn.hargreaves@manchester.ac.uk;

Contributing authors: sarah.woolner@manchester.ac.uk;

oliver.jensen@manchester.ac.uk;

Abstract

During cell division, the mitotic spindle moves dynamically through the cell to position the chromosomes and determine the ultimate spatial position of the two daughter cells. These movements have been attributed to the action of cortical force generators which pull on the astral microtubules to position the spindle, as well as pushing events by these same microtubules against the cell cortex and membrane. Attachment and detachment of cortical force generators working antagonistically against centring forces of microtubules have been modelled previously (Grill et al. 2005, *Phys. Rev. Lett.* **94**:108104) via stochastic simulations and Fokker–Planck equations to predict oscillations of a spindle pole in one spatial dimension. Using systematic asymptotic methods, we reduce the Fokker–Planck system to a set of ordinary differential equations (ODEs), consistent with a set proposed by Grill et al., which provide accurate predictions of the conditions for the Fokker–Planck system to exhibit oscillations. In the limit of small restoring forces, we derive an algebraic prediction of the amplitude of spindle-pole oscillations and demonstrate the relaxation structure of nonlinear oscillations. We also show how noise-induced oscillations can arise in stochastic simulations for conditions in which the Fokker–Planck system predicts stability, but for which the period can be estimated directly by the ODE model.

Keywords: mitotic spindle dynamics, stochastic simulation

1 Introduction

Embryos develop, on the most basic level, as a result of one cell dividing into two cells. In a tissue, the orientation of cell division is an important factor in determining either the outcome for the daughter cells (e.g. cell fate due to distribution of intracellular components or the daughter cell local environment) or the tissue as a whole (e.g. building tissue and organ architecture by tissue stratification or spreading) (Bergstralh and St Johnston, 2014; Morin and Bellaïche, 2011). Cell division orientation is determined by the mitotic spindle, the large microtubule-based structure which forms in the cell and segregates genetic material into two discrete daughter cells (Karsenti and Vernos, 2001; Mitchison and Salmon, 2001). Prior to anaphase, where the chromosomes are pulled apart to opposite ends of the cell, the mitotic spindle is positioned translationally and rotationally (Figure 1).

Key to spindle positioning is the pushing and pulling of astral microtubules which reach between the spindle pole and the cell cortex (Dogterom et al, 2005; Burakov et al, 2003; Zhu et al, 2010; Pecreaux et al, 2006; Howard, 2006; Okumura et al, 2018; Bosveld et al, 2016; Pecreaux et al, 2016). Pulling is mediated at the cell cortex through interactions between astral microtubules and the motor protein dynein, which is anchored at the plasma membrane through its association with a tripartite complex consisting of NuMA, LGN and Gai (Okumura et al, 2018; Bosveld et al, 2016; Pecreaux et al, 2016). Mathematical models have been utilised to investigate how astral microtubule pushing and pulling can drive spindle positioning. For example, minimising the calculated torque, created by pulling forces along the microtubule length (Minc et al, 2011) or by concentrated populations of dynein-associated proteins at the cell periphery (Théry et al, 2007; Bosveld et al, 2016), has been shown to predict the cell division orientation in sea urchin zygotes (Minc et al, 2011), micropattern-adhered HeLa cells (Théry et al, 2007) and the *Drosophila* pupal notum epithelium (Bosveld et al, 2016). These models highlight the importance of cell geometry (Minc et al, 2011) and the localisation of dynein (Théry et al, 2007; Bosveld et al, 2016) in spindle orientation and consequently cell division orientation. In a different approach, Li and Jiang (2017) used a stochastic model to describe the interactions of microtubules with chromosomes, motor proteins and boundaries to create self-assembled spindles within cells. This model was adapted to investigate spindle orientation: microtubules and chromosomes self-assemble into a mitotic spindle and orient within the simulated cells as a result of a combination of microtubule pushing forces and dynein-mediated pulling forces at both the cortex and within the cytoplasmic domain (Li et al, 2019), resulting in spindles which align with sites of localised dynein similarly to what has been shown in simpler models (Théry et al, 2007; Bosveld et al, 2016). Interestingly, the simulated spindles were shown to form already in line with their final division axis, with no notable movements of the spindle once assembled.

However, the mitotic spindle has been observed to approach its final destination less directly after its assembly. During the first division of the *C. elegans* fertilised egg, the posterior spindle pole undergoes a defined oscillation as the mitotic spindle is asymmetrically positioned in the cell to produce two daughter cells of unequal sizes (Pecreaux et al, 2006, 2016). Similarly, the rotational movements of the spindle in *Xenopus* epithelial tissue have been shown to be dynamic, culminating in oscillations

of the spindle angle immediately prior to anaphase (Larson and Bement, 2017). In the developing airway epithelium of mice, a subset of cells have been identified which continuously change their mitotic spindle angle throughout metaphase (Tang et al, 2018).

In the context of highly coordinated spindle movements, such as the oscillation of the *C. elegans* zygote posterior pole, contributions from both microtubule pushing and dynein-mediated pulling have been shown mathematically to produce the observed oscillatory dynamics (Grill et al, 2005; Pecreaux et al, 2006). This mathematical model describes changes in the position of the mitotic spindle pole in 1D as a result of pulling by cortical force generators, combined with microtubule-based restoring forces (Grill et al, 2005). The relative simplicity of this model compared with that used by Li and Jiang (2017) lends itself more readily to an investigation of the primary parameters giving rise to dynamic movements and, crucially, replicates the oscillations seen in *C. elegans*. The balance of microtubule pushing and dynein-mediated pulling forces are likely the drivers for producing spindle movements and subsequently for determining the division orientation.

Other cells demonstrate spindle movements which are more complex. By mathematical amplification of pulling forces on the mitotic spindle from discrete cortical locations, rotational spindle dynamics have been simulated to match those observed in HeLa cells (Corrigan et al, 2015). Stochastic switching between active and non-active cortical cues simulates noisy rotation toward the long axis of the cell as defined by anisotropy in the placement of the cortical locations (Corrigan et al, 2015), highlighting both the importance of cortical cue elements in spindle orientation and the possibility of stochasticity in creating dynamic movements of the spindle. Stochastic processes can result in behaviours which are not captured by deterministic models due to processes such as stochastic resonance (Erban and Chapman, 2020). Indeed, the addition of noise inherent to biological systems (Tsimring, 2014) should not be discarded in considerations of dynamic behaviour.

In *Xenopus* embryo epithelial tissue, mitotic spindles have been shown to undergo both a net rotation towards the final division axis and a stereotypical oscillation prior to anaphase onset (Larson and Bement, 2017) (see Online Resource 1). Figure 1(b-d) illustrates such oscillations in *Xenopus* animal cap epithelial tissue by tracking the movement of the metaphase plate, with which mitotic spindle movements are highly correlated. Oscillations are noisy with a nonlinear structure suggestive of relaxation oscillations (with rapid reversals of direction, Figure 1d), a feature not observed in the *C. elegans* spindle oscillation (Pecreaux et al, 2006). However, the factors which affect the structure of oscillations in the mitotic spindle, specifically the nonlinear structure identified in Figure 1(d), have not yet been fully described. Furthermore, spindles which do not oscillate are also present (Figure 1e,f), in contrast to the defined and characteristic spindle behaviour of the *C. elegans* zygote (Pecreaux et al, 2006, 2016). It is unclear how more complex tissue environments, such as is found in the *Xenopus* epithelium, may affect the ability of mitotic spindles to oscillate, or the non-linearity of the oscillatory spindle movements, motivating the present study of spindle dynamics.

In this paper, we revisit the mathematical model presented by Grill et al (2005), investigating factors which promote relaxation and noise-driven oscillations. The

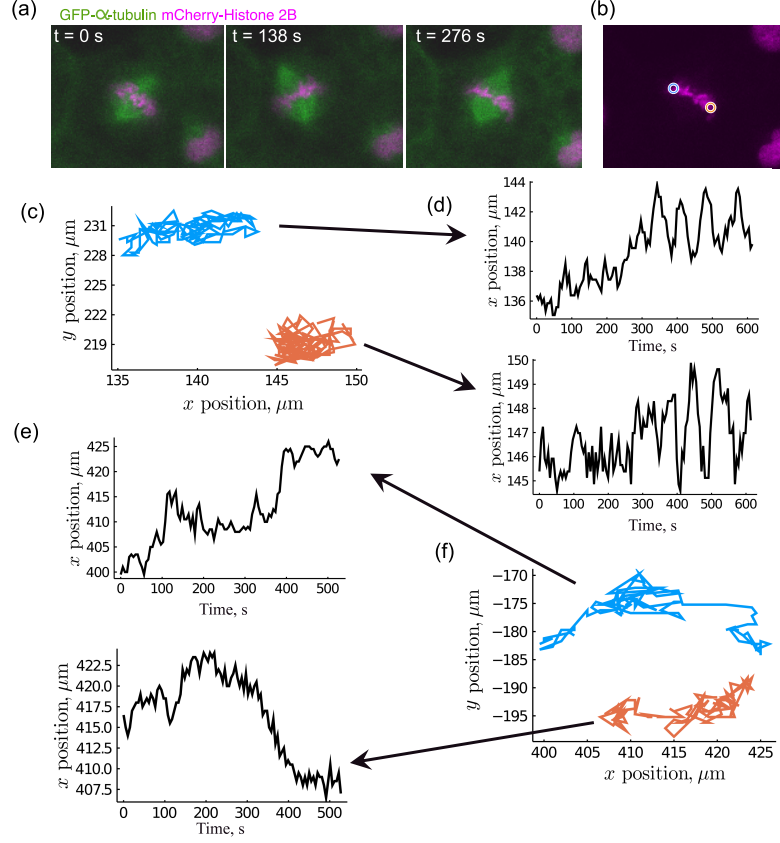


Fig. 1 The mitotic spindle and metaphase plate oscillate during the metaphase stage of mitotic cell division. (a) Time-lapse images of a mitotic spindle (GFP- α -tubulin, green) and metaphase plate (mCherry-Histone 2B, magenta) during metaphase of a cell dividing in a *Xenopus laevis* embryo, at stage 10-11. The metaphase plate lies perpendicular to the fusiform shape of the mitotic spindle. (b) Blue and orange circles indicate the measured termini of the metaphase plate. (c, f) Tracked positions of metaphase-plate termini over a full course of metaphase, for two cells in an excised *Xenopus* animal cap at stage 10-11. (d) The x -components of the termini tracked in (c), showing oscillatory motion as a function of time. (e) The x -components of the termini of the metaphase plate tracked in (f), showing non-oscillatory motion as function of time. Arrows indicate the relevant measured terminus. Data from [Hargreaves \(2023\)](#), obtained using methods described in [Appendix A](#).

model is outlined in [Section 2](#) and stochastic simulations are presented in [Section 3](#). Representations of solutions using Fokker–Planck equations are given in [Section 4](#), which are then reduced to a set of ordinary differential equations (ODEs) using systematic asymptotic analysis in [Section 5](#). These turn out to represent a special case of the (less formally derived) ODEs proposed by [Grill et al \(2005\)](#). A stability analysis gives predictions for the period of oscillation at the onset of neutral oscillations, as well as the position of the neutral oscillation boundary in parameter space, in

agreement with Fokker–Planck predictions. Further asymptotic reduction of the ODE model (Section 6) yields a single algebraic equation which describes the structure of nonlinear relaxation oscillations. We provide evidence that smaller amplitude irregular oscillations, characteristic of observations (Figure 1), can be induced by noise through stochastic resonance.

2 The model of spindle pole dynamics

In the 1D model of spindle pole dynamics proposed by Grill et al (2005), a spindle pole at position $\bar{z}(\bar{t})$ at a time \bar{t} moves along an axis $\hat{\mathbf{z}}$ spanning a cell according to

$$\bar{\xi} \frac{d\bar{z}}{d\bar{t}} + k_{\text{MT}} \bar{z}(\bar{t}) = \bar{F}^+ - \bar{F}^-. \quad (1)$$

The parameter $\bar{\xi}$ models viscous drag on the pole from the cytoplasm. The stiffness parameter k_{MT} represents a restoring force towards the cell midplane, arising from dynamic instability and bending of astral microtubules that emanate from the spindle pole and extend to the cell cortex (Grill et al, 2005; Pecreaux et al, 2006, 2016; Howard, 2006; Rubinstein et al, 2009). The spindle is pulled towards either side of the cell under fluctuating forces $\bar{F}^\pm(\bar{t})$. Pulling arises from individual force generators which lie at the cell cortex and bind to astral microtubules. For simplicity, the model considers two opposing populations of force generators which sit in an ‘upper’ and ‘lower’ cortex, labelled \pm hereafter. The force generators comprise a motor protein head connected to the cortex via an elastic linker of stiffness k_g (Figure 2). The motor protein head can be considered to be dynein, which binds to and walks along the microtubules towards the spindle pole. The two populations of N force generators are assumed to exert pulling forces toward their respective cortex with a magnitude

$$\bar{F}^\pm(\bar{t}) = k_g \sum_{n=1}^N \bar{y}_b^{(n)\pm}(\bar{t}), \quad (2)$$

where $\bar{y}_b^{(n)\pm}(\bar{t})$ is the extension of the elastic linker of bound (subscript b) force generator n . In (2) it is assumed that the pulling force due to an individual linker is proportional to its length. Unbound (subscript u) force generators of length $\bar{y}_u^{(n)\pm}$ (Fig. 2c) are not connected to the spindle pole and are unable to provide any forcing. The superscript (n) in (2) is used to label the n_b^\pm linkers that, in any short interval $(\bar{t}, \bar{t} + \delta\bar{t})$, are bound to a microtubule, where $0 \leq n_b^\pm \leq N$.

The forcing in (1) fluctuates because the linkers bind and unbind randomly. The movements of the spindle pole are tightly coupled to the individual extension lengths of the linkers via (2), and by the fact that spindle motion influences the length of bound linkers. The motor protein heads have walking velocities given by

$$\bar{v}_b^{(n)\pm} = v_0 \left(1 - \frac{k_g \bar{y}_b^{(n)\pm}}{f_0} \right) \mp \frac{d\bar{z}}{d\bar{t}}. \quad (3a)$$

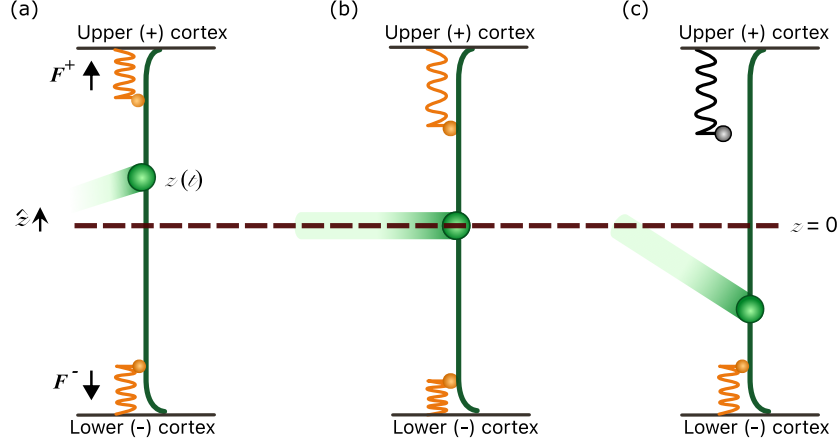


Fig. 2 Diagram of a spindle pole in three states. (a) The spindle pole (green) lies between the upper and lower cortex, displaced a distance $z(t)$ from the mid-point. Force generators (orange) at each cortex comprise a motor protein head and an elastic linker which produce pulling forces F^\pm . (b) Movement of the spindle pole affects the linker extensions of the motor proteins: movement away from the upper cortex lengthens the linkers of the upper force generators while compressing the linkers of the lower force generators. (c) Force generators with more extended linkers have an increased unbinding rate. Unbound generators cannot produce a pulling force (indicated by a grey force generator).

Here f_0 is the stall force of a force generator, i.e. the force required to bring the motor protein head to rest relative to the spindle pole; it is assumed that the unloaded walking velocity v_0 is reduced in proportion to $k_g \bar{y}_b^{(n)\pm} / f_0$, the tensile force acting upon the motor protein head by the elastic linker scaled relative to f_0 . Equivalently, $y_0 \equiv f_0 / k_g$ is the extension of a linker at which it stalls. In (3a), the spindle pole velocity term $\mp d\bar{z}/d\bar{t}$ arises due to the force generator being connected to the moving spindle pole via the microtubules. Thus, as the spindle pole moves towards a bound force generator it will compress the elastic linker by pushing on the bound motor, reducing its relative walking velocity (Figure 2). After a linker detaches from a microtubule, becoming unbound, it contracts with velocity

$$\bar{v}_u^{(n)\pm} = -(k_g / \bar{\xi}_g) \bar{y}_u^{(n)\pm}, \quad (3b)$$

where $\bar{\xi}_g$ is a drag coefficient of unbound dynein. Using the largest proteins in the force generator complex (dynein, length approximately 50 nm (Trokter et al, 2012), and NuMA, length approximately 210 nm (Compton and Cleveland, 1993)), a force generator has a Stokes radius of order 10^{-1} smaller than the spindle pole, so that $\bar{\xi}_g \approx \bar{\xi} \times 10^{-1}$. The superscript (n) in (3b) is used to label the n_u^\pm linkers that, in the short interval $(\bar{t}, \bar{t} + \delta\bar{t})$, are unbound, where $0 \leq n_u^\pm \leq N$ and $n_u^\pm + n_b^\pm = N$.

The model is closed by relating linker lengths to linker velocities, incorporating noise in the linker dynamics through effective diffusion coefficients \bar{D}_u and \bar{D}_b , and by modelling the transitions between bound and unbound states as random events taking

Description	Parameter	Value	Reference
Drag coefficient	$\bar{\xi}$	10^{-6} Nsm^{-1}	1
Microtubule stiffness	k_{MT}	$4 \times 10^{-6} \text{ Nm}^{-1}$	1, 2
Elastic linker stiffness	k_g	$8 \times 10^{-5} \text{ Nm}^{-1}$	1
Stall force	f_0	$3 \times 10^{-12} \text{ N}$	1, 3, 4
Spontaneous velocity of force generators	v_0	$1.8 \times 10^{-6} \text{ ms}^{-1}$	1, 5
Stall rate	v_0/y_0	50 s^{-1}	1
Retraction rate of unbound generators	$k_g/\bar{\xi}_g$	10^3 s^{-1}	(1, 6, 7)
Sensitivity of unbinding to linker extension	$\bar{\gamma}$	$5.6 \times 10^7 \text{ m}^{-1}$	(1)
Diffusion coefficient of bound generators	\bar{D}_b	$5 \times 10^{-15} \text{ m}^2\text{s}^{-1}$	1
Diffusion coefficient of unbound generators	\bar{D}_u	$5 \times 10^{-14} \text{ m}^2\text{s}^{-1}$	(1)
Number of force generators per cortex	N	-	
Maximum linker extension	\bar{y}_{max}	$2.16 \times 10^{-7} \text{ m}$	(1)
Microtubule-generator binding rate	$\bar{\omega}_{\text{on}}$	0.15 s^{-1}	
Microtubule-generator unbinding rate coefficient	$\bar{\omega}_0$	0.05 s^{-1}	1

Table 1 Parameter values and descriptions. References in parenthesis contain information which was used in order to derive the parameter value. References: 1 [Grill et al \(2005\)](#); 2 [Rubinstein et al \(2009\)](#); 3 [Belyy et al \(2014\)](#); 4 [Ezber et al \(2020\)](#); 5 [Milo and Phillips \(2015\)](#); 6 [Harborth et al \(1995\)](#); 7 [Trokter et al \(2012\)](#)

place at rates $\bar{\omega}_{\text{on}}$ and $\bar{\omega}_0 \exp[\bar{\gamma}\bar{y}_b^{(n)\pm}]$ respectively. Here $\bar{\gamma}$ parametrizes the slip-like manner in which dynein detaches from microtubules under loading ([Ezber et al, 2020](#)). Estimated values of dimensional parameters are summarized in Table 1.

Scaling lengths on the stall length y_0 and time on the stall time y_0/v_0 (so that $\bar{z} = y_0 z$, $\bar{t} = (y_0/v_0)t$, etc.), the force balance on the spindle pole (1, 2) becomes, in dimensionless form,

$$\xi \frac{dz}{dt} = -Kz(t) + \left(\sum_{n'=1}^N y_b^{(n')\pm}(t) - \sum_{n=1}^N y_b^{(n)\pm}(t) \right). \quad (4)$$

$\xi = \bar{\xi}v_0/(k_g y_0)$ and $K = k_{\text{MT}}/k_g$ are dimensionless drag and stiffness parameters respectively. The velocities of the bound and unbound generators (3a) become

$$v_b^{(n)\pm} = 1 - y_b^{(n)\pm} \mp \frac{dz}{dt}, \quad v_u^{(n)\pm} = -\Gamma y_u^{(n)\pm}, \quad (5)$$

where $\Gamma = f_0/(\bar{\xi}_g v_0)$. This parameter measures $k_g/\bar{\xi}_g$, the retraction rate of unbound linkers, relative to v_0/y_0 , the stall rate. Dimensionless counterparts of the stochastic

Parameter	Components	Baseline value
ξ	$\bar{\xi}v_0/f_0$	0.625
K	k_{MT}/k_g	0.05
ω_{on}	$\bar{\omega}_{\text{on}}y_0/v_0$	0.003
ω_0	$\bar{\omega}_0y_0/v_0$	0.001
y_{max}	\bar{y}_{max}/y_0	6
γ	$\bar{\gamma}y_0$	2
D_{b}	$\bar{D}_{\text{b}}/(y_0v_0)$	0.08
D_{u}	$k_{\text{b}}T/(v_0f_0)$	0.04
Γ	$f_0/(\bar{\xi}_gy_0)$	20

Table 2 Nondimensional parameters are given in terms of dimensional parameters. Baseline values are used in figures below, except where indicated. $k_{\text{b}}T$ is the unit of thermal energy.

parameters are diffusion coefficients D_{b} and D_{u} for bound and unbound linkers respectively, and transition rates ω_{on} and $\omega_0 e^{\gamma y_{\text{b}}^{(n)\pm}}$ respectively. Dimensionless parameters are summarised in Table 2.

Over any short interval, the populations of bound and unbound linkers have a distribution of lengths. Average extensions are defined by

$$\langle y_{\text{b(u)}}^{\pm} \rangle = \frac{\sum_{n=1}^N y_{\text{b(u)}}^{(n)\pm}}{n_{\text{b(u)}}^{\pm}}. \quad (6)$$

3 Stochastic simulations

To capture the discrete interactions between a small number of force generators and the spindle pole, we discretize $y_{\text{b}}^{(n)\pm}$ in increments of Δy and use a Gillespie algorithm to model the stochastic extensions and retractions of bound and unbound linkers and the stochastic transitions of the binding state of the force generators, as they bind and unbind from microtubules. As explained in Appendix B, the extension and retraction of the force generators are treated as $2N$ biased random walks with drift $v_{\text{b(u)}}^{\pm}$, diffusion $D_{\text{b(u)}}$ and state change (between bound and unbound states), all coupled to displacement of the spindle.

Figure 3 presents a simulation displaying the emergence of spontaneous oscillations of the spindle pole, using the parameters shown in Table 1, with $N = 15$ linkers at

either cortex. The spindle location (Figure 3a), numbers of bound and unbound force generators $n_{b(u)}^\pm$ (Figure 3b) and average extensions $\langle y_{b(u)}^\pm \rangle$ (6) (Figure 3b,c) show noisy but oscillatory dynamics. The average extensions of the bound force generators $\langle y_b^+ \rangle$ and $\langle y_b^- \rangle$ (6) oscillate in anti-phase to one another (Figure 3b). The average extension of unbound force generators $\langle y_u^\pm \rangle$ remains close to 0 following initial transients (Figure 3b). This can be explained by considering the movement of the spindle pole through one cycle of oscillation (Figure 3a) and $\langle y_b^\pm \rangle(z)$ (Figure 3c), discussed further below. Apparent gaps in the $\langle y_b^\pm \rangle$ plots (Figure 3c) occur where there are no bound generators from which to extract an average (where $n_b = 0$ in Figure 3b).

Consider the following phases of movement identified by coloured symbols in Figures 3(a, c).

1. **Spindle moving away from the upper cortex (green to cyan).** At the peak of the spindle pole oscillation, movement of the spindle is dominated by the microtubule restoring force. The bound generators are extended equally in the upper and lower cortices ($\langle y_b^+ \rangle \sim \langle y_b^- \rangle$ at the green timepoint (Figure 3c)) though there are a greater number bound in the upper cortex rather than the lower ($n_b^+ > n_b^-$, comparison in Figure 3bi vs bii). The restoring force ($-Kz$) is greater than the net upward pulling force provided by this unbalanced population ratio. As the spindle pole moves towards $z = 0$, this restoring force decreases while the increasing spindle pole velocity results in a net compression of the elastic linkers on the lower cortex, due to a switch in the sign of v_b^- ($\langle y_b^- \rangle$). Additionally, the spindle pole velocity increases the relative velocity of the force generators in the upper cortex, resulting in an extension of the elastic linkers at the upper cortex (Figures 3c), and shortening of the linkers at the lower cortex. Due to the tension-sensitive unbinding rate $\omega_0 e^{\gamma y_b^+}$, this results in a gradual decrease in the number of upper bound force generators as $\langle \omega_0 e^{\gamma y_b^+} \rangle$ increases in value, while the number of bound force generators in the lower cortex increases due to a constant binding rate and a decreased unbinding rate (Figure 3b).
2. **Spindle moving through the centre of its oscillating range, toward the lower cortex (cyan to yellow).** As the spindle moves through $z = 0$ the restoring force steadily increases from 0 to $-Kz$. This slows the movement of the spindle such that the velocity of the force generators in the lower cortex may become positive v_b^- ($\langle y_b^- \rangle$) > 0 which allows these elastic linkers to extend (Figure 3c), decreasing the relative velocity of the remaining upper force generators, the average extension of which is also reduced due to the unbinding of those with larger extensions and binding of force generators with reduced extensions (Figure 3c). The number of bound generators in the lower cortex also begins to decline as they extend due to the increased unbinding rate (Figure 3bii).
3. **Spindle moving away from the lower cortex (yellow to magenta).** This phase replicates the first phase, but with the behaviours of upper and lower cortex reversed. The motion away from the cortex due to the restoring force results in a compression of the upper elastic linkers and an extension of the lower elastic linkers (Figure 3c), and a corresponding decrease in the absolute number of bound force generators in the lower cortex as opposed to the increased binding observed in the upper cortex (Figure 3b).

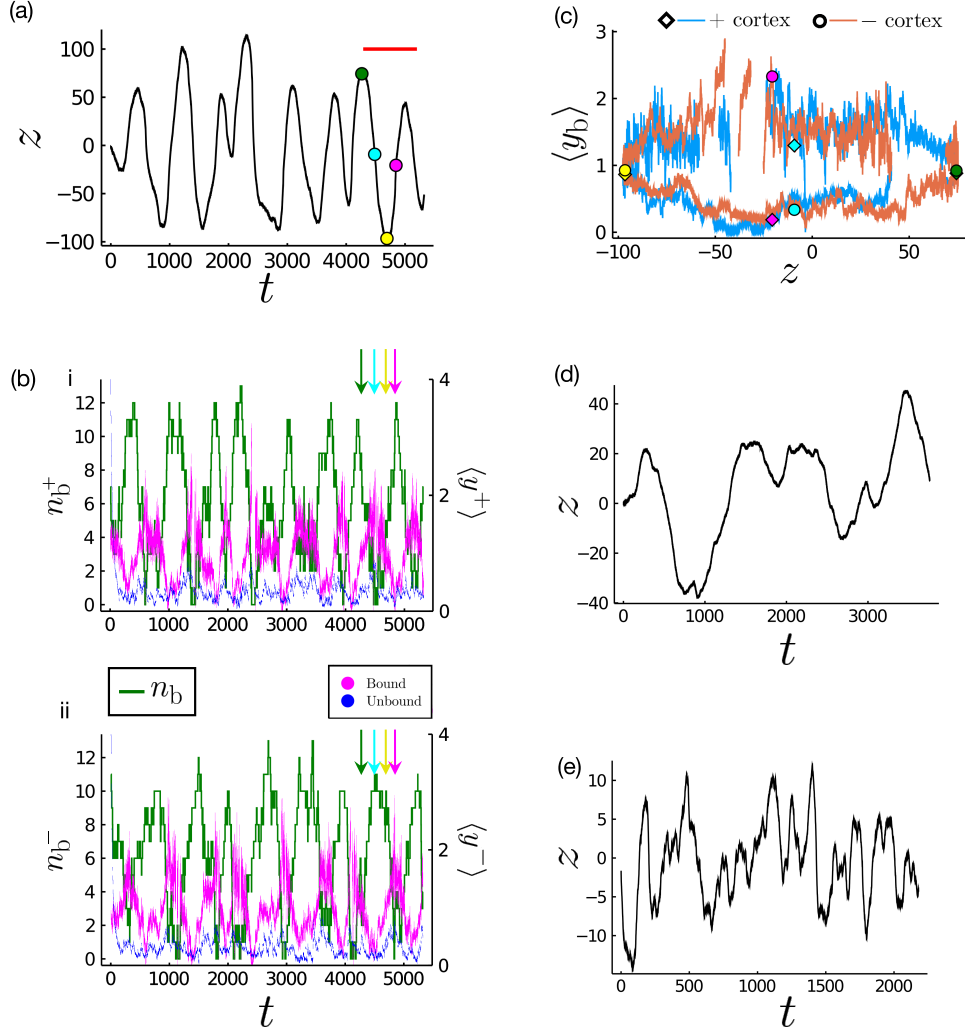


Fig. 3 Stochastic simulations can predict spontaneous oscillations of the spindle pole position. (a) Evolution of the non-dimensionalised spindle pole position through time. Dots correspond to moments in the cycle of interest and correspond colour-wise with the dots and diamonds plotted in (c). The red bar identifies the oscillation period predicted by (18b) below. (b) The number of bound force generators (green) in the i) upper (+) and ii) lower (-) cortex (left y -axis) through time. The average extensions of the bound (magenta) and unbound (blue) force generators in the i) upper (+) and ii) lower (-) cortex are also shown (right y -axis). Coloured arrows correspond temporally to coloured symbols in (a). (c) Average extension of the bound generators in the upper (blue) and lower (orange) cortices as a function of pole position. Parameters in (a,b,c) are as in Table 2 with $N = 15$. (d) A simulation when the unbinding of the force generator is no longer tension-sensitive, with $\gamma = 0$. (e) A simulation when the restoring force is increased by a factor of 100 to $K = 5$.

The closed loops in $(\langle y_b^\pm \rangle, z)$ space are traced anti-clockwise in the lower cortex and clockwise in the upper cortex (Figure 3c). At the stall force (when $\langle y_b^\pm \rangle \approx 1$), the direction of the solution loop is determined by the direction of acceleration of the spindle pole with respect to the cortex. That is, a force generator in the lower cortex whose elastic linker is at $y_b^{(n)\pm} = 1$ will be decreasing its extension as the spindle pole accelerates toward it (negative acceleration, green point in Figure 3(a,c)) and increasing as the spindle pole accelerates away (positive acceleration, yellow point in Figure 3(a,c)).

Removing the tension sensitivity of unbinding by setting $\gamma = 0$ results in less well-defined oscillations (Figure 3d) of reduced amplitude relative the baseline case shown in Figure 3(a). Thus the tension-sensitive unbinding rate appears to promote coherent oscillations of the spindle pole, although fluctuations persist due to the stochastic binding and unbinding. Similarly, increasing the restoring force by increasing the parameter K reduces the deviation in the position of the spindle pole from the centre (Figure 3e), but also leads to a marked reduction in the coherence of the spindle motion (compare Figure 3a and e).

4 A Fokker–Planck description

Simulating the system stochastically reveals the role of noise in individual realisations of spindle dynamics. To explore properties of the model over multiple realisations in a more computationally efficient manner, we turn to a system of partial differential equations (PDEs) for probability density functions (pdfs) $P_{b(u)}(y, t)$ for the extensions of bound and unbound linkers at either cortex, where the elastic linker extension y is now considered as a continuous variable. The model may be written as

$$P_{b,t}^\pm + J_{b,y}^\pm = \omega_{on} P_u^\pm - \omega_0 e^{\gamma y} P_b^\pm, \quad J_b^\pm = v_b^\pm P_b^\pm - D_b P_{b,y}^\pm, \quad (7a)$$

$$P_{u,t}^\pm + J_{u,y}^\pm = -\omega_{on} P_u^\pm + \omega_0 e^{\gamma y} P_b^\pm, \quad J_u^\pm = v_u^\pm P_u^\pm - \Gamma D_u P_{u,y}^\pm, \quad (7b)$$

where

$$v_b^\pm = 1 - y \mp \frac{dz}{dt}, \quad v_u^\pm = -\Gamma y. \quad (8)$$

Equation (7) is a nondimensional version of the Fokker–Planck equations proposed by Grill et al (2005). The continuous velocities $v_{b(u)}^\pm(y)$ in (8) evolve as in (5). The pulling force toward each cortex (2) is calculated as

$$F^\pm = N \int_0^{y_{\max}} y P_b^\pm(y, t) dy, \quad (9)$$

modifying the force balance on the spindle (4), which becomes

$$\xi z_t = -Kz - N \left(\int_0^{y_{\max}} y P_b^- dy - \int_0^{y_{\max}} y P_b^+ dy \right). \quad (10)$$

The boundary conditions

$$J_b^\pm = J_u^\pm = 0 \quad \text{at } y = 0 \text{ and } y = y_{\max}, \quad (11)$$

ensure conservation of total probability

$$\int_0^{y_{\max}} (P_b^\pm + P_u^\pm) dy = 1. \quad (12)$$

Given some initial conditions $P_b^\pm(y, 0) = P_{b0}^\pm(y)$, $P_u^\pm(y, 0) = P_{u0}^\pm(y)$, and $z(0) = z_0$, the system (7–11) may be solved in time to return the dynamics of the spindle pole and the populations of cortical force generators, represented as probability densities over multiple realisations of the system. We computed numerical solutions using the method of lines.

The solutions presented in Figure 4 show an oscillating spindle displacement $z(t)$ corresponding to fluctuations in $P_b^\pm(y, t)$ and $P_u^\pm(y, t)$. For large Γ , (7b) is dominated by the advective term which sweeps any unbound force generators with a non-zero extension down toward $y = 0$. As there is no flux through this boundary by (11), P_u^\pm has a defined peak at $y = 0$ which decays with y over the diffusive lengthscale $D_u^{1/2}$. For the bound pdfs P_b^\pm , the location y_c^\pm and amplitude $P_b^{\pm, \max}$ of the maximum of the pdf oscillate concurrently with z (Figure 4c, g), mirroring the behaviour of the average extension $\langle y_b^\pm \rangle$ and number of bound force generators n_b^\pm in the stochastic simulation (Figure 3b). Variations of the initial conditions P_{b0}^\pm and P_{u0}^\pm had no effect on the final solutions following initial transients (data not shown).

Decreasing D_b and D_u by a factor of 10 results in taller and narrower pdfs (Figure 4d, h), confining P_b^\pm to a region of y which is spatially separated from P_u^\pm at all times. In this limit we can partition the y -domain into three distinct regions: I, of width $\mathcal{O}(D_u^{1/2})$, encompassing the peak of P_u^+ ; III, of width $\mathcal{O}(D_b^{1/2})$, encompassing the peak of P_b^+ ; and II between them, which remains distinct throughout an entire oscillation (Figure 4h, see Online Resource 2c). As well as modulating the shape of the pdfs, D_b and D_u also affect the resulting dynamics of the spindle pole. Decreasing D_b and D_u results in an increased period, T , of oscillation ($T \approx 890$ increases to $T \approx 1000$ upon a decrease in D_b and D_u by a factor of 10), a decrease in the amplitude of the oscillation (Figure 4a, e) and longer transients (Figure 4a, e).

The solution in Figure 4(a–d) was run with parameters matching those in the stochastic simulation in Figure 3, except that $N = 25$ in the former and $N = 15$ in the latter. Nevertheless, PDE predictions show a comparable period, without capturing the detailed fluctuations in an individual realisation. To obtain a broader view of parameter dependence, solutions of (7–11) for a range of values of N and ω_{on} are reported in Figure 5(a). For the baseline value $\omega_{\text{on}} = 0.003$, sustained oscillations arise in the PDE model with $N = 25$ and low diffusivities (as in Figure 4e–h) but not $N = 15$ (see Figure 5c). Increasing diffusivities with $N = 15$ leads to the sustained oscillations seen in the PDE model in Figure 5(d). Noise, therefore, is likely to play a role in promoting oscillatory dynamics.

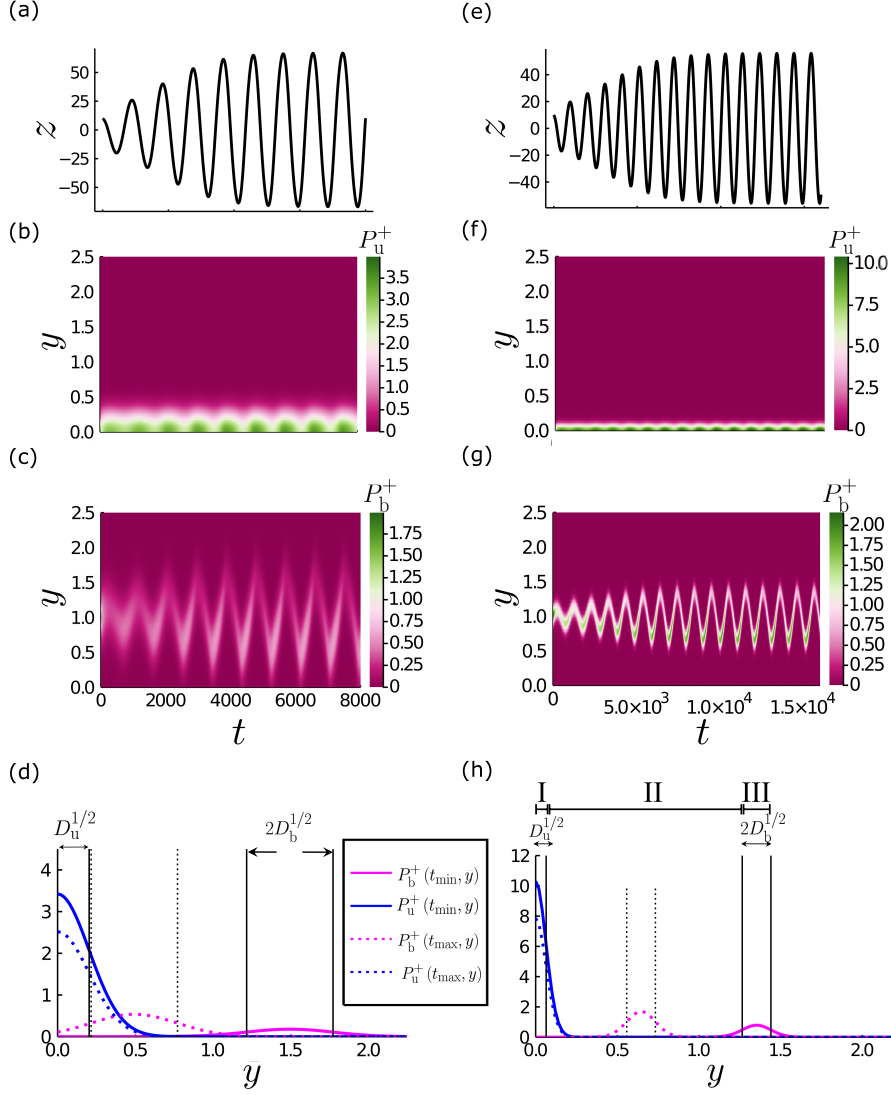


Fig. 4 The effect of varying the magnitude of diffusion in the Fokker–Planck description. (a,e) Example solution to equations (7a, 7b, 10), showing the pole position, z versus time t . Diffusion parameters D_b, D_u are a factor of 10 smaller in the right column than in the left column. (b,f) Heat map of $P_u^+(y, t)$. (c,g) Heat map of $P_b^+(y, t)$. (d,h) Probability density functions in the upper cortex at two instances of time. Solid lines: $t = t_{\min}$, when the spindle pole is at $z = 0$ and moving toward its minimum value ($z_t < 0$). Dotted lines: $t = t_{\max}$, when the spindle pole is at $z = 0$ and moving toward its maximum value ($z_t > 0$). The peak widths scale with $D_u^{1/2}$ and $D_b^{1/2}$ as indicated. (h) The three regions used to reduce the system of PDEs to ODEs are indicated by roman numerals I, II, and III. The behaviour of the pdfs in the lower cortex are in antiphase to the behaviour seen here. Solutions were obtained using parameters as in Table 2 plus: $N = 25$; (a-d) baseline diffusivities $D_b = 0.08$, $D_u = 0.04$; (e-h) $D_b = 8 \times 10^{-3}$, $D_u = 4 \times 10^{-3}$.

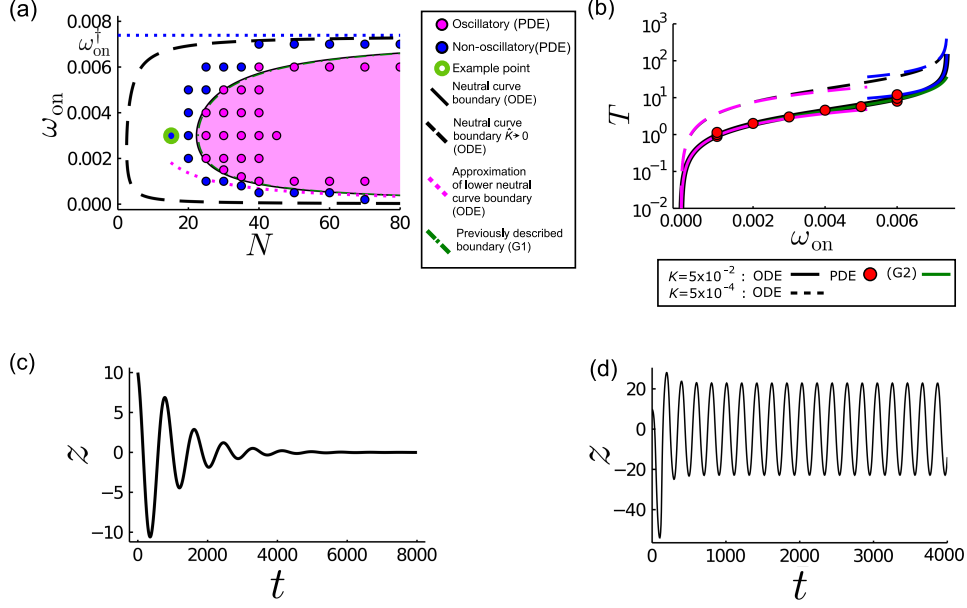


Fig. 5 The stability boundary between oscillatory and non-oscillatory solutions is affected by the magnitude of diffusive terms. (a) Numerically solving the Fokker-Planck system (circles) reveals a boundary in (N, ω_{on}) space which separates oscillatory from non-oscillatory solutions. Each circle represents a numerical solution, labelled magenta if the spindle pole has sustained oscillations and blue if the spindle pole position decays to $z = 0$ for large t . The point with the green boundary is the location in parameter space at which the solutions (c) and (d) sit. Other parameters are as in Table 2 except that $D_b = 8 \times 10^{-3}$ and $D_u = 4 \times 10^{-3}$. The shaded magenta area represents the region where oscillatory solutions exist as determined by stability analysis of the ODEs (19b) using equivalent parameters. The dashed curve (black) shows the same threshold in the $\hat{K} \rightarrow 0$ limit determined by (21). The dotted magenta curve shows the asymptote of the lower boundary for $N \gg 1$ and $N\omega_{on} = \mathcal{O}(1)$, as in (24). The dashed green curve shows the stability boundary (G1) predicted by (20b) from Grill et al (2005). (b) The relationship between the period of oscillation and the binding rate ω_{on} using (19a), along the neutral stability curve (19b). The period is unbounded as $\omega_{on} \rightarrow \omega_{on}^\dagger$. Points denote the periods taken from PDE solutions along the approximate neutral curve identified in Figure 5a. The magenta curves represent the approximations to the period for small $\bar{\omega}_{on}$ as in (25). The blue curves represent the approximations to the period as $\omega_{on} \rightarrow \omega_{on}^\dagger$ as in (23). The dashed green curve shows the period (G2) predicted by (20a) from Grill et al (2005). (c) Spindle pole position z in time t at the example point (green in (a)), from a PDE solution. (d) A PDE solution replicating (c) except that $D_b = 8 \times 10^{-1}$ and $D_u = 4 \times 10^{-1}$.

The PDE stability boundary for low diffusivities is mapped out in (N, ω_{on}) -space (Figure 5a), distinguishing oscillatory from non-oscillatory solutions. The period of oscillation for neutrally-stable disturbances increases with ω_{on} (Figure 5b). Reduction of the number of force generators, leading to a decrease in pulling forces, results in a cessation of oscillations (Figure 5a,c). For large N , two thresholds exist for values of ω_{on} at which oscillations arise, with the oscillatory section of parameter space forming a wedge shape (Figure 5a). We explore the origins of these thresholds in more detail below. This wedge-shaped parameter space was described previously by Grill et al

(2005) through analysis of a reduced model where it was assumed that unbound force generators instantaneously relax down to zero extension. The presence of a threshold between oscillatory and non-oscillatory solutions has been experimentally validated in *C. elegans* embryos (Pecreaux et al, 2006).

Significantly, the oscillatory behaviour reported in stochastic simulations for $N = 15$ (Figure 3a), lies in a regime in which the Fokker–Planck model predicts steady distributions of $P_{b(u)}^\pm$ with $z \rightarrow 0$ at large times (Figure 5c). We provide evidence below that the sustained oscillations in Figure 3a are noise-driven (or a form of stochastic resonance (Erban and Chapman, 2020)).

Additional PDE solutions with low diffusivities are reported in Figure 6(a,c), illustrating respectively the impact of increasing N and decreasing the strength of the restoring force K . The latter leads to larger-amplitude oscillations with a relaxation structure, characterised by periods of approximately uniform spindle velocity, interspersed with rapid changes in direction (Figures 6c). Correspondingly, the oscillations combine slow phases in the time-evolution of P_b^\pm and y_c^\pm (Figure 6c) in which z is approximately linear in t , with short intervals in which the rapid change in the direction of motion of the spindle pole coincides with fast changes in the extension of the force generator bound probability centre y_c^\pm and amplitude P_b^\pm . We explore the origins of this strongly nonlinear behaviour below, through comparison to a simplified model reported in the remaining panels of Figure 6.

The Fokker–Planck description reveals the main characteristics promoting spindle-pole oscillations, but still requires extensive computation. We now reduce this model to a system of ODEs by asymptotic analysis, allowing us to more fully explore the relationships between the most important factors promoting oscillations. Rather than follow the heuristic approach proposed by Grill et al (2005), we seek a systematic reduction valid at an appropriate distinguished limit in parameter space.

5 Asymptotic reduction to ODEs

When diffusivities are small, the PDEs reveal distinct regions of y space where the pdfs P_u^\pm and P_b^\pm have most of their mass (Figure 4h). While varying the diffusive terms has an impact on the oscillations, with larger diffusive terms promoting oscillations (Figure 5d), the amplitudes and periods of the more and less diffusive solutions are still of a similar order. We now pursue the behaviour of the model with lower diffusivity to create a system of ODEs.

We develop an approximation to the oscillating spindle system in a distinguished limit for which $\omega_{\text{on}} \sim \omega_0 \sim D_b^{1/2} \sim D_u^{1/2} \ll 1$ (where \sim means ‘scales like’) and rescale the time and spindle position parameters in the PDE problem (7), (8) and (10) by $t = \tilde{t}/\omega_{\text{on}}$ and $z = \tilde{z}/\omega_{\text{on}}$. The range of extension values y are split into the three regions identified in Figure 4(h): I, over which P_u^\pm is peaked around $y = 0$ with a width $D_u^{1/2}$; III, over which P_b^\pm is peaked with a width of $D_b^{1/2}$ but whose centre moves as $y_c = 1 \mp \tilde{z}_t$; and II, where advective terms dominate.

In Appendix C, we express the governing equations in rescaled coordinates, expand in powers of ω_{on} , solve for P_u^\pm in region I and P_b^\pm in region III, and then match

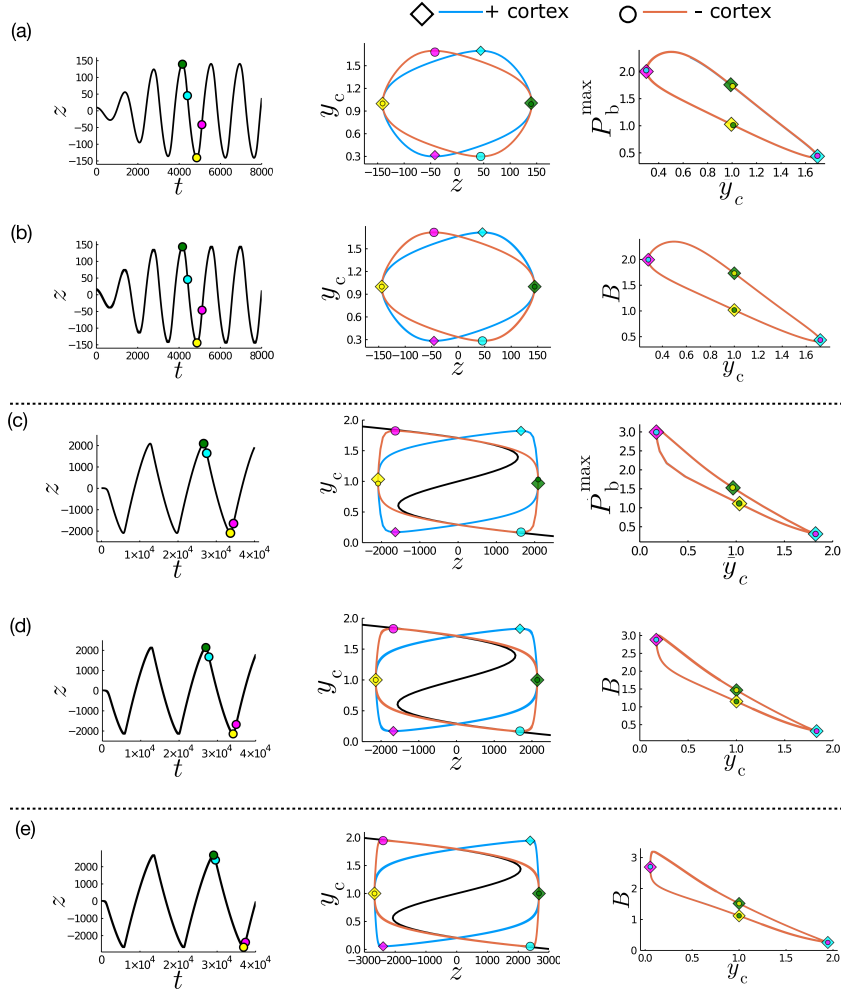


Fig. 6 Comparison of PDE (a, c) and ODE (solutions for equivalent parameters. PDE and ODE solutions for equivalent parameters are presented, with non-equivalent solutions separated by a dotted line. (a, c) solutions of the PDEs; (b, d, e) solutions of the ODEs. First column: spindle pole position z . Second column: centre of the bound pdf as a function of pole position $y_c^\pm(z)$. Third column: amplitude of the bound pdf as a function of the location of its peak ($P_b^\pm(y_c)$ for PDE solutions (a,c); $B^\pm = \hat{B}^\pm / \sqrt{2\pi D_b}$ for ODE solutions (b, d, e). PDE solutions were obtained using parameters are as in Table 2 except $D_b = 8 \times 10^{-3}$, $D_u = 4 \times 10^{-3}$, (a) $N = 45$ and (c) $K = 5 \times 10^{-4}$ and $N = 15$. ODE solutions obtained using (b) equivalent parameters to (a); (d) equivalent parameters to (c); and (e) Equivalent parameters to (a) with $N = 1500$. Line colours correspond to solutions in each cortex (blue = upper, orange = lower). The black curves in the centre column represent the predicted limit cycle as $\hat{K} \rightarrow 0$, as determined by the inversion of (30). Scatterpoints denote the positions of: maximum amplitude (blue $z > 0$, yellow $z < 0$), maximum spindle pole velocity (cyan $z_t < 0$, magenta $z_t > 0$).

asymptotic limits across region II. This procedure yields the three coupled ODEs

$$\left(\hat{\xi} + \hat{B}^+ + \hat{B}^-\right) \ddot{z}_t + \hat{K} \dot{z} = \hat{B}^+ - \hat{B}^-, \quad (13a)$$

$$\left(1 + \rho e^{\gamma(1 \mp \ddot{z}_t)}\right) \dot{\hat{B}}^\pm + \hat{B}_t^\pm = 1. \quad (13b)$$

Here $\hat{B}^\pm(\hat{t}) = \sqrt{2\pi D_b} B^\pm$, where B^\pm approximates the amplitude of the peak of P_b^\pm . The parameters in (13) are

$$\rho = \frac{\omega_0}{\omega_{\text{on}}} = \frac{\bar{\omega}_0}{\bar{\omega}_{\text{on}}}, \quad \hat{\xi} = \frac{\xi}{N} = \frac{\bar{\xi} v_0}{f_0 N}, \quad \hat{K} = \frac{K}{N \omega_{\text{on}}} = \frac{k_{\text{MT}} v_0}{N \bar{\omega}_{\text{on}} f_0}. \quad (14)$$

Formally, the parameters (14) are assumed to remain $\mathcal{O}(1)$ in the limit $\omega_{\text{on}} \sim \omega_0 \sim D_b^{1/2} \sim D_u^{1/2} \ll 1$. ρ is the binding affinity (under zero load) of force generators for microtubules; $\hat{\xi}$ measures the spindle drag (assuming the spindle moves at the walking speed of a linker) relative to the stall force generated by the full population of linkers; \hat{K} measures the restoring force, driving the spindle to the centre of the cell (assuming a displacement of the spindle comparable to the distance walked by a linker), relative to the stall forces generated by the full population of linkers. We solved (13) numerically, imposing initial conditions \ddot{z}_0 and \hat{B}_0^\pm .

The ODEs defined by Grill et al (2005) may be re-written in the notation used above as

$$\hat{\xi} \ddot{z}_t + \hat{K} \dot{z} = \hat{B}^+ \tilde{y}^+ - \hat{B}^- \tilde{y}^- \quad (15a)$$

$$\left(1 + \rho e^{\gamma \tilde{y}^\pm}\right) \dot{\hat{B}}^\pm + \hat{B}_t^\pm = 1 \quad (15b)$$

where \tilde{y}^\pm , the typical length a linker extends before it detaches, is determined from

$$\mp \ddot{z}_t = \left(\omega_0 e^{\gamma \tilde{y}^\pm} + 1\right) \tilde{y}^\pm - 1. \quad (15c)$$

Assuming $\omega_0 \ll 1$ in (15c), then $\tilde{y} \simeq 1 \mp \ddot{z}_t$ and we recover (13). Our asymptotic reduction therefore recovers a special case of the heuristically-determined ODEs presented by Grill et al (2005).

In Figure 6(a-d), two solutions of the Fokker-Planck system are compared with solutions of the ODEs (13) for equivalent parameters, taking $y_c^\pm = 1 \mp \ddot{z}_t$. The spindle pole dynamics and associated force generator behaviours in both cortices are fully captured in the ODE model in both cases.

Relaxation oscillations arise when pulling forces dominate over restoring forces, through a reduction of \hat{K} . Figure 6(c,d) shows a strong match between the relaxation oscillations returned by the PDE and ODE models for an equivalent reduction in K , with similar period and amplitude as well as shape. Likewise applying an increase in N (Figure 6e), the ODE model predicts a strong relaxation structure (with very sharp changes in y_c^\pm at the peaks of oscillation). Thus we conclude that the balance of pulling to restoring forces controls the structure of the oscillation of the spindle pole.

Interestingly, the oscillations in the lower- \hat{K} and high- N relaxation oscillation are slightly different. For low \hat{K} , the peak of the bound pdf hits its maximum at the same time as the spindle pole experiences its maximum velocity (when y_c^\pm is at its minimum value, Figure 6c,d). Alternatively, when N is increased (leading to changes in \hat{K} and $\hat{\xi}$), the maximum of the peak of the bound pdf lags behind the spindle pole velocity (Figure 6e). This lag represents a delay between the binding of the force generators and the movements of the spindle pole, likely due to there being a greater number of force generators in the system to bind to the microtubules before saturation of the force generators onto the microtubule. Indeed when ω_{on} is small, the oscillations of the spindle pole are more non-linear (data not shown), as the number of bound force generators takes longer to saturate.

5.1 Stability analysis

The simplicity of the ODE model (13) lends itself to stability analysis. Linearising about the steady state

$$\hat{B}^{*\pm} = \lambda^{-1}, \quad \hat{z}^* = 0, \quad \lambda \equiv 1 + \rho e^\gamma, \quad (16)$$

assuming that small disturbances are proportional to e^{st} , yields the relationship

$$(s + \lambda) \left(s^2 + s \left(\lambda + \frac{\hat{K}\lambda}{\lambda\hat{\xi} + 2} - \frac{2\gamma(\lambda - 1)}{\lambda\hat{\xi} + 2} \right) + \frac{\hat{K}\lambda^2}{\lambda\hat{\xi} + 2} \right) = 0. \quad (17)$$

Setting $s = \mu + i\Omega$ and collecting real and imaginary parts defines the growth rate

$$\mu = \frac{2\gamma(\lambda - 1) - \hat{K}\lambda - \lambda(\lambda\hat{\xi} + 2)}{2(\lambda\hat{\xi} + 2)} \quad (18a)$$

and frequency of oscillation

$$\Omega^2 = \frac{\hat{K}\lambda^2}{\lambda\hat{\xi} + 2} - \frac{1}{4} \left(\frac{\hat{\xi}\lambda + \hat{K} - 2\left(\frac{\gamma}{\lambda}(\lambda - 1) - 1\right)}{\hat{\xi} + 2/\lambda} \right)^2. \quad (18b)$$

Setting $\mu = 0$ at the onset of neutral oscillations identifies the frequency

$$\Omega^2 = \frac{\hat{K}\lambda^2}{2 + \hat{\xi}\lambda} \quad (19a)$$

and the stability threshold

$$\hat{K} = 2 \left(\frac{\gamma}{\lambda}(\lambda - 1) - 1 \right) - \hat{\xi}\lambda. \quad (19b)$$

Both (19b) and (19a) provide good predictions of the stability boundary identified by PDE solutions (Figure 5a) and the period of oscillations at the stability boundary (Figure 5b).

The frequency of oscillation determined by Grill et al (2005) via (15) may be rewritten using the notation above as

$$\Omega^2 = \frac{\hat{K}\lambda^2(1 + (\gamma + 1)\omega_0 e^\gamma)}{\hat{\xi}\lambda(1 + (\gamma + 1)\omega_0 e^\gamma) + 2} \quad (20a)$$

at the stability threshold

$$\hat{K} = \frac{2\left(\frac{\gamma}{\lambda}(\lambda - 1) - 1\right)}{\omega_{\text{on}}(\lambda - 1)(\gamma + 1) + 1} - \hat{\xi}\lambda. \quad (20b)$$

Equations (20a) and (20b) are equivalent to (19a) and (19b) respectively when $\omega_0 \sim \omega_{\text{on}} \ll 1$. (19b) and (20b) are compared in Figure 5(a), showing a near-perfect match despite the additional terms present in (20b); both predictions bound almost perfectly the oscillatory region observed by individual solutions of the PDEs.

We highlight two limits of (19b). First, taking $\hat{K} \rightarrow 0$, leaving $\hat{\xi} = \xi/N$ as the only parameter which depends on N , (19b) reduces to

$$N = \frac{\xi\lambda^2}{2\gamma(\lambda - 1) - 2\lambda} = \frac{\xi(\omega_{\text{on}} + \omega_0 e^\gamma)^2}{2\omega_{\text{on}}[\omega_0 e^\gamma(\gamma - 1) - \omega_{\text{on}}]}, \quad (21)$$

provided the denominator $2[\gamma(\lambda - 1) - \lambda]$ is positive, i.e.

$$\omega_{\text{on}} < \omega_{\text{on}}^\dagger \equiv (\gamma - 1)\omega_0 e^\gamma. \quad (22)$$

In this limit, the period of oscillation $T = 2\pi/\Omega$ is

$$T \approx 2\pi \left(\frac{(\gamma - 1)N\omega_{\text{on}}^\dagger}{K\gamma} \right)^{1/2}. \quad (23)$$

$\omega_{\text{on}} \rightarrow \omega_{\text{on}}^\dagger$ also appears in the large- N limit of (19b), taking $\hat{K} \sim \hat{\xi} \ll 1$. In addition, taking $N \gg 1$, $\omega_{\text{on}} \ll 1$ with $N\omega_{\text{on}} = O(1)$, we recover the additional approximation (provided $\gamma > 1$)

$$\omega_{\text{on}} \approx \frac{K + \xi\omega_0 e^\gamma}{2N(\gamma - 1)} \quad (24)$$

for which

$$T = 2\pi \frac{\omega_{\text{on}}}{\omega_{\text{on}}^\dagger} \left[\frac{(\gamma - 1)(K + 2\xi\omega_0 e^\gamma)}{K} \right]^{1/2}. \quad (25)$$

Thus, for large N , the upper branch of the stability boundary defined by (19b) in Figure 5(a) approaches $\omega_{\text{on}} = \omega_{\text{on}}^\dagger$ in (22), confirming that a necessary condition for oscillations is that the tension-sensitivity parameter satisfies $\gamma > 1$, i.e. that linkers exhibit slip-bond behaviour. Indeed, removal of the tension-sensitivity of the unbinding

rate in the stochastic simulations leads to a reduction of the coherence of the oscillatory behaviour of the spindle pole (Figure 3d). The upper-branch asymptote $\omega_{\text{on}} = \omega_{\text{on}}^\dagger$ appears to be shared also by PDE solutions (which suggests an upper stability threshold between $0.006 < \omega_{\text{on}}^\dagger < 0.007$ for $N \leq 80$, within 80% of $\omega_{\text{on}}^\dagger = 0.0074$). Also in the large- N limit, the lower branch of (19b) is captured by (24), consistent with PDE solutions in this limit. This limit shows explicitly how increasing the restoring force K has a stabilising effect.

We also recall that, in the Fokker–Planck model, decreasing the restoring force parameter K promotes oscillations at smaller N (Figure 6c, where $N = 15$). This behaviour is conserved in the ODE system, where the low- \hat{K} approximation (21) shown in Figure 5(a), predicts oscillations in a greater region of the (N, ω_{on}) -plane. Evaluating $d\omega_{\text{on}}/dN$ using (21) gives

$$\frac{dN}{d\omega_{\text{on}}} = 0 \quad \text{on} \quad \frac{\omega_{\text{on}}}{\omega_{\text{on}}^\dagger} = \frac{N - (\xi/(\gamma - 1))}{2N + \xi}. \quad (26)$$

Thus for the neutral curve to lie in $N > 0$ requires

$$N > \frac{\xi}{\gamma - 1} \equiv \frac{\bar{\xi}v_0}{f_0(\gamma - 1)}, \quad (27)$$

providing a lower bound on the number of linkers needed for oscillations in terms of the walking speed and stall force of a linker, and the drag on the spindle.

The period of oscillations along the neutral stability curve predicted using (19a) increases as K decreases (Figure 5b); thus a reduction of restoring forces corresponds to longer periods of oscillation. The rapid increase of the period as $\omega_{\text{on}} \rightarrow \omega_{\text{on}}^\dagger$ coincides with $N \rightarrow \infty$. (19a) is well matched with (20b) determined by Grill et al (2005), as well as with the periods along the approximate stability curve identified by numerical solutions of the PDEs.

Finally, we can use the ODE solution to provide further evidence that the oscillations in Figure 3(a) are noise-induced. Despite lying outside the neutral curve (Figure 5a), the period of the stochastic oscillations is well approximated by (18b) (Figure 3a, red bar), indicating that noise due to the relatively small number of linkers is sufficient to overcome the damping evident in the Fokker–Planck description (Figure 5c) and in the ODE model. As explained in Appendix B, the Fokker–Planck system (7, 10) proposed by Grill et al (2005) is a simplified form of the high-dimensional chemical Fokker–Planck equation associated with the full stochastic model; we attribute the failure of (7, 10) to predict the oscillations in Figure 3(a) to this simplification.

6 The structure of relaxation oscillations

A further simplification to the model can be implemented by exploiting \hat{K} as a small parameter. The approximately linear sections of \tilde{z} (e.g. Figure 4c) scale like \hat{K}^{-1} in both time and amplitude, and are interrupted by rapid changes in spindle direction.

Re-scaling $\tilde{t} = \hat{t}/\hat{K}$ and $\tilde{z} = \hat{z}/\hat{K}$ such that $\tilde{z}_{\tilde{t}} = \tilde{z}_{\tilde{t}}$, the ODEs (13) describing the slower phases of the dynamics become

$$\left(1 + \rho e^{\gamma(1 \mp \tilde{z}_{\tilde{t}})}\right) \hat{B}^{\pm} + \hat{K} \hat{B}_{\tilde{t}}^{\pm} = 1, \quad (28a)$$

$$\left(\hat{\xi} + \hat{B}^+ + \hat{B}^-\right) \tilde{z}_{\tilde{t}} + \tilde{z} = \hat{B}^+ - \hat{B}^-. \quad (28b)$$

Posing expansions $\hat{B}^{\pm} = \hat{B}_0^{\pm} + \hat{K} \hat{B}_1^{\pm} + \dots$ and $\tilde{z} = \tilde{z}_0 + \hat{K} \tilde{z}_1 + \dots$, to leading order (28) becomes

$$\left(1 + \rho e^{\gamma(1 \mp \tilde{z}_{0,\tilde{t}})}\right) \hat{B}_0^{\pm} = 1, \quad (29a)$$

$$\left(\hat{\xi} + \hat{B}_0^+ + \hat{B}_0^-\right) \tilde{z}_{0,\tilde{t}} + \tilde{z}_0 = \hat{B}_0^+ - \hat{B}_0^-. \quad (29b)$$

We may rewrite (29b) as

$$\tilde{z}_0 = \hat{B}_0^+ - \hat{B}_0^- - \left(\hat{\xi} + \hat{B}_0^+ + \hat{B}_0^-\right) \tilde{z}_{0,\tilde{t}} \equiv G\left(\tilde{z}_{0,\tilde{t}}\right), \quad (30)$$

with \hat{B}_0^{\pm} defined by (29a).

Equation (30) approximates the slow phases of the limit cycle in $(\tilde{z}_0, \tilde{z}_{0,\tilde{t}})$ as $\hat{K} \rightarrow 0$. Recalling that $y_c^{\pm} = 1 \mp z_t$, then following a parameter rescaling, (30) can also be used to describe the limit cycle in (z_0, y_c^{\pm}) (black curve in Figure 6c-e). The limit cycles obtained by solving the ODE and PDE systems with equivalent parameters are shown to closely match with this expected limit cycle (Figure 6c-e). These cycles show the fast phases of the relaxation oscillation as the spindle pole changes its direction of motion (the approximately vertical sections at the maximum and minimum values of \tilde{z}). The maximum amplitude of oscillation can be estimated by the roots of G , which can be determined by solving

$$\frac{dG}{d\tilde{z}_{0,\tilde{t}}} = 0. \quad (31)$$

for roots G_{\max} and G_{\min} . Then the amplitude of oscillation during relaxation oscillations can be estimated by

$$\tilde{z} \approx (G_{\max} - G_{\min})/\hat{K}. \quad (32)$$

Thus the amplitude of oscillation can be estimated from the ratio of pulling to pushing (\hat{K}), the effective drag ($\hat{\xi}$), the ratio of the unbinding to binding rates (ρ) and the tension sensitivity of unbinding (γ).

This approximation also illustrates how the tension-sensitivity of the cortical force generators, mediated by γ , is key for oscillations. Setting $\gamma = 0$ in (29a) uncouples the values of \hat{B}_0^{\pm} from the spindle pole dynamics, thus $\hat{B}_0^+ = \hat{B}_0^-$ and (29b) becomes $\tilde{z}_0 = -\left(\hat{\xi} + 2(1 + \rho)^{-1}\right) \tilde{z}_{0,\tilde{t}}$, giving a linear relationship between \tilde{z}_0 and $\tilde{z}_{0,\tilde{t}}$ and

eradicating the limit cycle. Thus the coupling of the populations of bound force generators through the tension-sensitive unbinding rate is required for oscillations, as was shown by stability analysis of the ODE system (22).

7 Discussion

We have investigated the factors promoting relaxation and noise-driven oscillations of the mitotic spindle identified experimentally (Figure 1), by revisiting the mathematical model proposed by Grill et al (2005). To this end, we used stochastic simulations to demonstrate the effect of noise on 1D pole movement (Section 3, Figure 3); this involved $2N$ random walkers (linkers) switching between bound and unbound states, with their motion coupled via an ODE to that of the spindle. The corresponding Fokker–Planck equations (Section 4, Figure 4), involving four PDEs coupled to an ODE, were reduced systematically (Section 5) to three nonlinear ODEs (13). These turn out to be a special (and simpler) case of the ODE system presented by Grill et al (2005), and they show close agreement with the Fokker–Planck solutions in predicting conditions necessary for the onset of self-excited oscillations (Figure 5a). Further asymptotic reduction revealed the single algebraic equation describing the slow dynamics of the nonlinear relaxation oscillations and the associated amplitude of oscillation (Section 6, Figure 6c-e).

While there is consistency between the descriptions in many respects, a striking feature is the appearance in stochastic simulations of noise-induced oscillations in a regime predicted to be linearly stable by the Fokker–Planck description (and the associated ODE system). The oscillations arise close to a stability boundary, and their period is well predicted by analysing the three linearised ODEs (the green circle in Figure 5(a) highlights the position in parameter space occupied by the stochastic solution in Figure 3a; the period prediction is given by (18b)). The amplitude of the oscillations is likely to be regulated by the noise associated with stochastic linker dynamics. It is feasible that the linearised ODEs might be generalised to a set of stochastic differential equations, with forcing dependent (for example) on the fluctuating number of bound linkers and their transition rates. We leave derivation of these equations as a task for the future. We can however consider instances where experimentally observed oscillations may be driven by noise: the predicted period of oscillation can then be used to infer (or at least constrain estimates of) some of the parameters relevant to the *Xenopus* system. For example, for parameters as in Table 1, for a period of $T \approx 100$ s as seen experimentally (Figure 1d) then $N = 175$ force generators would be required. However, if restoring forces were reduced to $K = 0.005$ then $N = 21$ force generators would be required to achieve the same period. These would result in oscillations with an amplitude of $\approx 15 \mu\text{m}$ which is comparable with the typical size of a cell ($\approx 20 \mu\text{m}$ diameter) though approximately three to four times larger than what was recorded experimentally (Figure 1d, $\approx 2\text{--}5 \mu\text{m}$).

Figure 5(c,d) shows how increasing demographic stochasticity by increasing the value of diffusive terms D_b and D_u can promote oscillations. Thus, noise increases the ease with which oscillations are sustained. Expansion of regions of parameter space giving rise to oscillatory solutions under the addition of noise has been seen elsewhere,

in studies of oscillations in protein expression. For example, [Phillips et al \(2016\)](#) show that stochasticity increases the robustness of the oscillatory phenotype of gene expression resulting in the correct timing of cell differentiation. Indeed, if oscillations of the spindle pole play an important role in correctly orientating the mitotic spindle, then the inherent stochasticity of biological systems due to fluctuations in protein levels or ATP availability (driving dynein movement) would aid the robustness of correct spindle orientation.

Relaxation oscillations arise when restoring forces decrease relative to pulling forces (Figure 6c-e). Biologically, this may be achieved by reducing the restoring force, for example by hinging of microtubules at the spindle pole ([Howard, 2006](#); [Rubinstein et al, 2009](#)), or by increased numbers of dynein linkers at the cell cortex (denoted in this work by an increase in N). The resulting linear sections of the spindle pole oscillation align temporally with slow phases in the time-evolution of P_b^\pm and y_c^\pm (Figure 6c-e), until the spindle pole is sufficiently displaced from the centre for the restoring force to create a rapid reversal in the spindle pole velocity z_t . This change in the spindle pole velocity results in a rapid increase in the value of y_c on the opposite cortex, which in turn creates a rapid decrease in the value of P_b^\pm due to the tension-sensitivity of the unbinding rate. P_b^\pm and y_c^\pm have amplitudes that are self-limited by the tension-sensitive unbinding, and amplified by their connection to the motion of the spindle pole. We have shown that $\gamma > 1$ is required for oscillations to occur at all (e.g in (22), (24)); dynein’s slip-bond ([Ezber et al, 2020](#)) is crucial for oscillatory dynamics, but the sensitivity of the slip-bond to tension may affect the nonlinearity of the oscillation.

In the limit of small restoring forces, the model may be simplified to a single algebraic equation describing the slow phases of the limit cycle in $(\tilde{z}_0, \tilde{z}_{0,\tilde{t}})$ and subsequently in (z_0, y_c^\pm) , where the maximum amplitude of oscillation can be estimated using (32). However, re-dimensionalisation of the amplitude seen during relaxation oscillations (Figure 6c-e) results in an oscillation with an amplitude of order ≈ 0.1 mm (for chosen baseline parameters), which is an order of 10 larger than the typical size of a cell in the *Xenopus* epithelium ($\approx 20 \mu\text{m}$ diameter). Then in the cell we may conclude that restoring forces are not vanishingly small and that more complex dynamics may be at play to create relaxation oscillations, for example a nonlinear restoring force.

While we have studied a 1D model, imaged mitotic spindles in epithelial cells show 2D dynamics (Figure 1; Online Resource 1), with forces acting on both spindle poles originating from the entire cell periphery. To properly consider the spindle dynamics and infer *Xenopus* system specific parameters, the relative motion of the two spindle poles must become part of the equation. The simplification of the present model to ODEs or low-dimensional SDEs is a key step to fully modelling 2D movements of a full mitotic spindle. From there, we may begin to piece together the full processes by which the mitotic spindle is positioned and orientated in tissue-based cells. In doing so, we must remain mindful that inherent stochasticity may increase the mobility of the spindle.

Supplementary information. Online Resource 1: Time-lapse of a dividing cell in the epithelium of a *Xenopus laevis* embryo at stage 10. The mitotic spindle is seen in green (GFP- α -tubulin) and metaphase plate in magenta (mCherry-Histone 2B). Images taken every $t = 6.0$ s.

Online Resource 2: a) Movie of the evolution of fluxes J_b^+ , J_u^+ and their sum $J_b^+ + J_u^+$. b) as in a) with a truncated y -axis to better demonstrate the dynamics of J_b^+ and $J_b^+ + J_u^+$. c) The evolution of the pdfs P_u^+ and P_b^+ . Parameter values as in Table 1 but with $D_b = 0.008$, $D_u = 0.004$ and $N = 25$.

Acknowledgments. The authors have applied a Creative Commons Attribution (CCBY) licence to any Author Accepted Manuscript version arising. This work was supported by the Wellcome Trust (098390/Z/12/Z and 225408/Z/22/Z). DH was supported by a Wellcome Trust PhD studentship (220054/Z/19/Z). OEJ and SW acknowledge support from the Leverhulme Trust (RPG-2021-394). The authors are grateful to Simon Cotter for technical advice.

Declarations

Author contributions. All authors contributed to the study conception and design. Mitotic spindle movie acquisition was performed by SW. Imaging of the metaphase plate and data analysis was performed by DH. The first draft of the manuscript was written by DH and all authors commented on subsequent versions of the manuscript. All authors read and approved the final manuscript.

Ethical approval. All work with *Xenopus laevis* was performed using protocols approved by the UK Government Home Office under the Home Office Project Licence PFDA14F2D (Holder: Professor Enrique Amaya) and Home Office Personal Licences held by SW and DH.

Availability of data and materials. Biological data available upon request.

Code availability. Code available as follows: Stochastic simulations (Section 3) at github.com/dionn-hargreaves/StochasticSimulation_SpindleMovements. Fokker-Planck equations (Section 4) at github.com/dionn-hargreaves/1Dspindle_FP_MoL. ODE equations (Section 5) at github.com/dionn-hargreaves/ODE_1D_spindle.

Appendix A Acquisition of biological data

Xenopus laevis *Xenopus laevis* male and female frogs were housed within tanks maintained by the in-house animal facility at the University of Manchester. Female frogs were pre-primed 4-7 days in advance of embryo collection by injection with 50 U of pregnant mare serum gonadotrophin (Intervet UK) into the dorsal lymph sac. One day prior to embryo collection, male and pre-primed female frogs were primed by injection with 100 U (male) and 200 U (female) of human chorionic gonadotrophin (hCG; Chorulon, MSD) into the dorsal lymph sac. 2-5 h ahead of embryo collection, primed male and female frogs were transferred into the same tank for amplexus. Embryos were collected over 1 h time periods. Embryos were dejellied with 2% L-cysteine solution (Sigma Aldrich, #168149-100G) in 0.1X Marks Modified Ringers (MMR) [1X MMR: 100mM NaCl, 2mM KCl, 1mM MgCl₂, 1mM CaCl₂, 0.5mM EDTA and 5mM HEPES, pH7.8], rinsed with 0.1X MMR and incubated at room temperature (RT) to reach two-cell stage.

All *Xenopus* work was performed using protocols approved by the UK Government Home Office and covered by Home Office Project License PFDA14F2D (License Holder: Professor Enrique Amaya) and Home Office Personal Licenses held by SW and DH.

A.1 Whole embryo movies, spindle and metaphase plate

For live imaging of mitotic spindles in *Xenopus* embryos (Figure 1a, b), both cells of two-cell embryos were microinjected with 5 nl of mRNA for GFP- α -tubulin (needle concentration of 0.5 g/l) and mCherry-Histone 2B (0.1 g/l), to highlight spindle microtubules and chromosomes, respectively. Embryos were incubated for 20 hours post fertilization at 16°C and then mounted for live imaging in 0.1X Marks Modified Ringers (MMR) [10X solution: 1 M NaCl, 20 mM KCl, 10 mM MgCl₂.6H₂O, 20 mM CaCl₂.2H₂O, 1 mM EDTA disodium salt, 50 mM Hepes, up to 5 L with distilled water], using a ring of vacuum grease to contain the embryos and support a glass coverslip as in Woolner et al (2010). Imaging took place at developmental stages 10–11. Single focal plane live-cell images of spindles were collected at RT (21°C) every 6 seconds using a confocal microscope (FluoView FV1000; Olympus) with FluoView acquisition software (Olympus) and a 60X, 1.35 NA U Plan S Apochromat objective. Time-lapse videos were constructed from the single focal plane images using ImageJ.

A.2 Animal cap movies, metaphase plate only

For imaging in the animal cap to follow dynamics of spindle movements (Figure 1c-f), both cells of two-cell embryos were microinjected with mRNA for mCherry-Histone 2B (0.1 g/l; to highlight chromosomes) and BFP-CAAX (0.1 g/l; to highlight cell edges) using a Picospritzer III Intracel injector (*Parker instrumentation*). Injected embryos were washed in 0.1% MMR and incubated in fresh 0.1% MMR overnight at 16°C. Animal cap explants were prepared from the injected embryos at the early gastrula stage (stage 10). The embryos were transferred to Danilchik's for Amy explant culture media (DFA) [53 mM NaCl, 5 mM Na₂CO₃, 4.5 mM Potassium gluconate, 32 mM Sodium gluconate, 1 mM CaCl₂, 1 mM MgSO₄, up to 1 L with MilliQ water, pH 8.3 with Bicine] in 0.1% BSA (*Sigma*, A7906). The vitelline membranes were removed from the embryos using forceps, and the explant removed by incisions with the forceps around the animal pole resulting in separation of the animal cap tissue from the embryo (Joshi and Davidson, 2010). The animal caps were then transferred onto a fibronectin-coated PDMS membrane with the basal side in contact with the membrane to prevent balling up and held in place with a coverslip. The caps were then left to recover for 2 hours at 18°C before imaging (Goddard et al, 2020).

The PDMS membranes were prepared as described previously (Goddard et al, 2020). The PDMS membrane was mounted onto a stretch apparatus (*custom made by Deben UK 722 Limited*) and subjected to a uniaxial stretch of 0.5 mm displacement to ensure that the membrane remained taut under gravity and the weight of the animal cap (Nestor-Bergmann et al, 2018). Images were acquired every 5 seconds on a Leica TCS SP8 AOBS upright confocal using a 20X dipping objective at 2X confocal zoom. The confocal settings were as follows: pinhole 1.9 airy unit, 600 Hz bidirectional

scanning, format 1024 x 1024. Images were collected using hybrid detectors with the detection mirror settings for red and blue at 600-690 nm, and 415-516 nm respectively, using the white light laser with excitation at 586 nm, and 405 nm laser lines. The images were collected non-sequentially with a z -spacing of 10 μm between sections. Images were taken continuously without resetting for drifting in order to ensure no missing data points for dividing cells. The maximum imaging duration per animal cap was 2 hours.

A.3 Spindle movement analysis

All images were processed and analysed on **ImageJ** (Schneider et al, 2012). All measurements were taken from maximum intensity projections of the z -stack images. Each end of the metaphase plate was tracked in each frame using the **ImageJ** multi-point tool, returning an x and y coordinate for each point. The centre of the cell at the beginning of metaphase, \mathbf{R}_1 , and the end of metaphase, \mathbf{R}_2 , were used to create a linear correction to the metaphase plate position across metaphase time. Cell edges and tricellular vertices were manually traced at the beginning and end of metaphase using the **ImageJ** 'Paintbrush tool' (brush width = 1 pixel). The manual traces were processed using in-house **Python** scripts to return the cell centre position (Nestor-Bergmann et al, 2018, 2019). The measurements were made based on the polygonised cell according to the positions of the tricellular vertices. Oscillations were detected from signals using a periodogram.

Appendix B Implementation of the Gillespie algorithm

The extension of an elastic linker is discretised into states $y_{b(u)}^{(n)\pm,i}$ with $i = 0, 1 \dots M$, separated by a fixed distance Δy such that $y_{b(u)}^{(n)\pm,i+1} = y_{b(u)}^{(n)\pm,i} + \Delta y$. Each force generator n has identifiers which denote the associated cortex (\pm), the current extension state (i), and the binding state (u for unbound, b for bound). The binding state will be identified in the subscript and written as $b(u)$, referring to a subscript b or u.

At any time, a generator may

- retract: $y_{b(u)}^{(n)\pm,i} \rightarrow y_{b(u)}^{(n)\pm,i-1}$ with probability $r_{b(u)}^{(n)\pm,i}$;
- extend: $y_{b(u)}^{(n)\pm,i} \rightarrow y_{b(u)}^{(n)\pm,i+1}$ with probability $f_{b(u)}^{(n)\pm,i}$; or
- switch between bound and unbound states: $y_b^{(n)\pm,i} \leftrightarrow y_u^{(n)\pm,i}$ with probability $s_{b(u)}^{(n)\pm,i}$.

These state-changing events are illustrated graphically in Figure B1a.

Probabilities $r_{b(u)}^{(n)\pm,i}$, $f_{b(u)}^{(n)\pm,i}$, and $s_{b(u)}^{(n)\pm,i}$ are related to model parameters as follows. The switching probabilities were chosen such that an unbound generator may switch to become a bound generator within a short time τ with a probability $s_u^{(n)\pm,i} = \tau\omega_{on}$ for a constant binding rate ω_{on} . In a short time τ , a bound generator may unbind with probability $s_b^{(n)\pm,i} = \tau\omega_0 e^{\gamma y_b^{(n)\pm,i}}$.

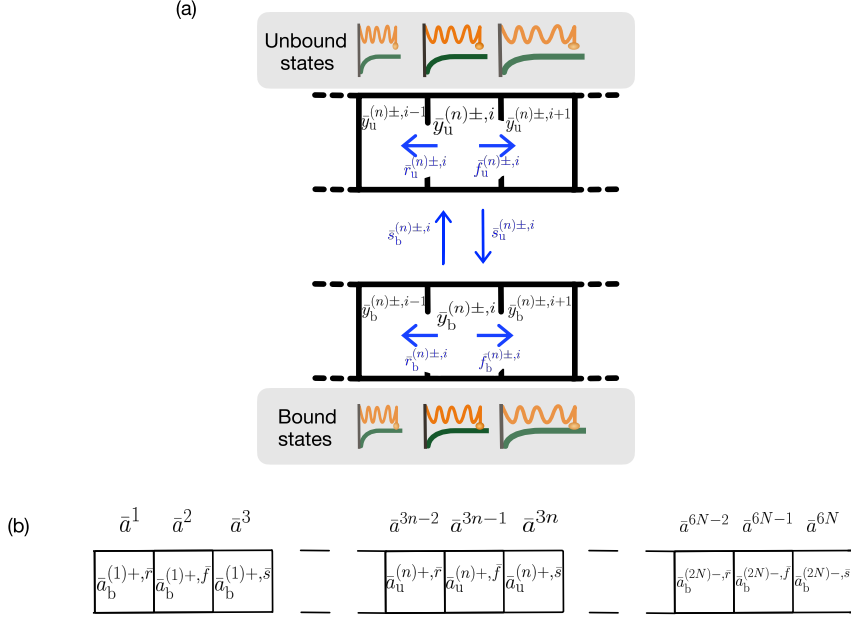


Fig. B1 Graphical map of extension states for unbound and bound force generators. (a) Unbound generators in state $y_u^{(n)\pm, i}$ may extend or retract with probabilities $f_u^{(n)\pm, i}$ and $r_u^{(n)\pm, i}$. Bound generators in state $y_b^{(n)\pm, i}$ may extend or retract with probabilities $f_b^{(n)\pm, i}$ and $r_b^{(n)\pm, i}$. Bound generators may unbind or vice-versa with rate constants $s_b^{(n)\pm, i}$ and $s_u^{(n)\pm, i}$ respectively. Diagrams of force generators show corresponding extension and binding states. Each individual force generator n exists within these states. (b) Concatenated list of rate triplets to show numbering scheme. Probabilities from a^1 to a^{3N} correspond to force generators $1 \rightarrow N$ which exist in the upper cortex. Probabilities a^{3N+1} to a^{6N} correspond to force generators $N+1 \rightarrow 2N$ which exist in the lower cortex.

In order to obtain expressions for $r_{b(u)}^{(n)\pm, i}$ and $f_{b(u)}^{(n)\pm, i}$, consider

$$v_{b(u)}^{(n)\pm, i} = \frac{\Delta y}{\tau} \left(f_{b(u)}^{(n)\pm, i} - r_{b(u)}^{(n)\pm, i} \right), \quad (\text{B1a})$$

$$D_{b(u)}^{(n)\pm} = \frac{(\Delta y)^2}{2\tau} \left(f_{b(u)}^{(n)\pm, i} + r_{b(u)}^{(n)\pm, i} \right), \quad (\text{B1b})$$

as an effective drift speed and diffusion coefficient for force generators respectively. These arise from considering extension or contraction of each linker as a biased random walk. We summarise these transition probabilities as

$$s_b^{(n)\pm, i} = \tau \omega_0 e^{\gamma y_b^{(n)\pm, i}}, \quad s_u^{(n)\pm, i} = \tau \omega_{on}, \quad (\text{B2a})$$

$$r_b^{(n)\pm,i} = \tau \left(\frac{D_b}{(\Delta y)^2} - \frac{v_b^{(n)\pm,i}}{2\Delta y} \right), \quad r_u^{(n)\pm,i} = \tau \Gamma \left(\frac{D_u}{(\Delta y)^2} + \frac{y_u^{(n)\pm,i}}{2\Delta y} \right), \quad (\text{B2b})$$

$$f_b^{(n)\pm,i} = \tau \left(\frac{D_b}{(\Delta y)^2} + \frac{v_b^{(n)\pm,i}}{2\Delta y} \right), \quad f_u^{(n)\pm,i} = \tau \Gamma \left(\frac{D_u}{(\Delta y)^2} - \frac{y_u^{(n)\pm,i}}{2\Delta y} \right). \quad (\text{B2c})$$

No flux conditions were enforced by setting $r_{b(u)}^{(n)\pm,i=0} = 0$ and $f_{b(u)}^{(n)\pm,i=M} = 0$.

The Gillespie algorithm (Gillespie, 1977) stipulates that the probability of a state-changing event (extension, retraction, or switch) happening within a short time τ is exponentially distributed with rates $r_{b(u)}^{(n)\pm,i}/\tau$, $f_{b(u)}^{(n)\pm,i}/\tau$, and $s_{b(u)}^{(n)\pm,i}/\tau$, which sum together to give a total rate

$$R = \frac{1}{\tau} \sum_{n=1}^{2N} \left(r_{b(u)}^{(n)\pm,i} + f_{b(u)}^{(n)\pm,i} + s_{b(u)}^{(n)\pm,i} \right). \quad (\text{B3})$$

Here $2N$ is the total number of force generators within the system (N per cortex), each of which is associated with either the upper (+) or lower (-) cortex, has an extension state i , and is either bound (b) or unbound (u). We assume that only one event for one force generator may occur, removing the possibility of simultaneous events. As $r_{b(u)}^{(n)\pm,i}$, $f_{b(u)}^{(n)\pm,i}$ and $s_{b(u)}^{(n)\pm,i}$ are proportional to the short time τ (B2), the rates $r_{b(u)}^{(n)\pm,i}/\tau$, $f_{b(u)}^{(n)\pm,i}/\tau$, and $s_{b(u)}^{(n)\pm,i}/\tau$ (and thus R) are independent of τ . A random variable ζ_1 is chosen from a uniformly random distribution between 0 and 1 ($\zeta_1 \sim \mathcal{U}[0, 1]$) and the time to the next event is calculated using $\tau = R^{-1} \log(1/\zeta_1)$. The rescaled rates $a_{b(u)}^{(n)\pm,r}(i) = R^{-1} r_{b(u)}^{(n)\pm,i}/\tau$, $a_{b(u)}^{(n)\pm,f}(i) = R^{-1} f_{b(u)}^{(n)\pm,i}/\tau$ and $a_{b(u)}^{(n)\pm,s}(i) = R^{-1} s_{b(u)}^{(n)\pm,i}/\tau$ are concatenated in triplets for each force generator n , giving a list of potential states a^j with $j \in [1, 6N]$ which sum together to give $\sum_{j=1}^{6N} a^j = 1$ (Figure B1b). Choosing an independent random variable from a uniformly random distribution, $\zeta_2 \sim \mathcal{U}[0, 1]$, the next state-changing event is determined as the first j such that $\sum_{j'=1}^j a^{j'} > \zeta_2$. Force generators in the upper (n^+) and lower (n^-) cortex have corresponding events a^j where $j \in [1, 3N]$ and $j \in [3N + 1, 6N]$ respectively.

In order to calculate the spindle pole position, we implement a forward Euler approximation of (4) which may be used to calculate the pole position at a time $t + \tau$,

$$z(t + \tau) = \left(1 - \frac{\tau K}{\xi} \right) z(t) + \frac{\tau}{\xi} \left(\sum_{n'=1}^{N'} y_b^{(n')+,i}(t) - \sum_{n=1}^N y_b^{(n)-,i}(t) \right). \quad (\text{B4})$$

Here n' and N' are the equivalent of n and N , introduced to separate the upper and lower cortex in this expression.

In summary, the state of the system at any instant can be described by a vector $\mathbf{X}(t)$ of size $\mathcal{N} = 1 + 4N(M + 1)$, comprising the spindle location plus the occupancies of $4N$ linkers (N at each cortex, in bound or unbound states) in states of different lengths (over a scale discretized into $M + 1$ elements). In principle such a system can be represented (Erban and Chapman, 2020) by a chemical master equation for $p(\mathbf{x}, t)$, the probability that $\mathbf{X}(t) = \mathbf{x}$, coupled (Langevin) stochastic differential equations for

the elements of \mathbf{X} and a chemical Fokker–Planck equation for $p(\mathbf{x}, t)$. The latter is a PDE of $\mathcal{N} + 1$ dimensions. This is distinct from the heavily reduced Fokker–Planck system (7,10) proposed by Grill et al (2005) that motivates the stochastic system illustrated in Figure B1.

Appendix C Reducing the Fokker–Planck equations to ODEs

To reduce the Fokker–Planck model to a system of ODEs, we rescale using the motor-protein-to-microtubule binding rate, writing $t = \tilde{t}/\omega_{\text{on}}$ and $z = \tilde{z}/\omega_{\text{on}}$. Then (10) and (7) become

$$\xi \tilde{z}_{\tilde{t}} = -\frac{K}{\omega_{\text{on}}} \tilde{z} - N \left(\int_0^{y_{\text{max}}} y P_{\text{b}}^- dy - \int_0^{y_{\text{max}}} y P_{\text{b}}^+ dy \right), \quad (\text{C5a})$$

$$\omega_{\text{on}} P_{\text{b}, \tilde{t}}^\pm + J_{\text{b}, y}^\pm = \omega_{\text{on}} P_{\text{u}}^\pm - \omega_0 e^{\gamma y} P_{\text{b}}^\pm, \quad (\text{C5b})$$

$$\omega_{\text{on}} P_{\text{u}, \tilde{t}}^\pm + J_{\text{u}, y}^\pm = -\omega_{\text{on}} P_{\text{u}}^\pm + \omega_0 e^{\gamma y} P_{\text{b}}^\pm. \quad (\text{C5c})$$

We develop an approximation to the oscillating spindle system for which $\omega_{\text{on}} \sim \omega_0 \sim D_{\text{b}}^{1/2} \sim D_{\text{u}}^{1/2} \ll 1$. To minimise the introduction of further notation, we expand our solutions in terms of the small order parameter ω_{on} and remain mindful that these parameters are taken to be of similar order. The range of extension values y is split into three regions (Figure 4h): region I over which P_{u}^\pm is peaked around $y = 0$ with a width $D_{\text{u}}^{1/2}$; region III over which P_{b}^\pm is peaked with a width of $D_{\text{b}}^{1/2}$ but whose centre moves as $y_{\text{c}} = 1 \mp \tilde{z}_{\tilde{t}}$; and region II where advective terms dominate and the asymptotic limits of I and III are matched. Solutions for P_{u}^\pm and P_{b}^\pm will be determined in regions I and III respectively, followed by matching their asymptotic limits in region II to reveal the ODE system which governs the time evolution of the parameters.

C.1 Region I

In Region I, we seek solutions $P_{\text{u}}^\pm \sim P_{\text{u}0}^\pm + \omega_{\text{on}} P_{\text{u}1}^\pm + \dots$ where $P_{\text{u}0}^\pm$ is a quasi-static solution whose shape is static but whose amplitude varies slowly in time. We assume further that $P_{\text{b}}^\pm \sim \omega_{\text{on}}$ in this region (Figure 4h). Here, it is observed that P_{u}^\pm is sharply peaked about $y = 0$ over a diffusive length-scale $D_{\text{u}}^{1/2}$ (Figure 4h). Thus, setting $y = D_{\text{u}}^{1/2} Y$ in (C5c) gives

$$\omega_{\text{on}} P_{\text{u}, \tilde{t}}^\pm - \Gamma \left(Y P_{\text{u}}^\pm + P_{\text{u}, Y}^\pm \right)_Y = -\omega_{\text{on}} P_{\text{u}}^\pm + \omega_0 e^{(\gamma D_{\text{u}}^{1/2} Y)} P_{\text{b}}^\pm \quad (\text{C6})$$

with the boundary condition $J_{\text{u}}^\pm(\tilde{t}, 0) = 0$. This boundary condition therefore becomes

$$J_{\text{u}0}^\pm(\tilde{t}, 0) + \omega_{\text{on}} J_{\text{u}1}^\pm(\tilde{t}, 0) = 0 \quad (\text{C7})$$

where

$$J_{u0}^{\pm} = -D_u^{-1/2} \Gamma \left(Y P_{u0}^{\pm} + P_{u0,Y}^{\pm} \right), \quad (\text{C8a})$$

$$J_{u1}^{\pm} = -D_u^{-1/2} \Gamma \left(Y P_{u1}^{\pm} + P_{u1,Y}^{\pm} \right), \quad (\text{C8b})$$

which are both individually zero at $Y = 0$ due to (C7). To leading order in ω_{on} , (C6) becomes

$$\Gamma \left(Y P_{u0}^{\pm} + P_{u0,Y}^{\pm} \right)_Y = 0 \quad (\text{C9})$$

which may be integrated to give $\Gamma \left[Y P_{u0}^{\pm} + P_{u0,Y}^{\pm} \right]_0^Y = 0$. Thus, due to boundary condition (C7),

$$Y P_{u0}^{\pm} + P_{u0,Y}^{\pm} = 0, \quad (\text{C10})$$

which gives

$$P_{u0}^{\pm} = A^{\pm}(\tilde{t}) e^{-\frac{1}{2}Y^2} \quad (\text{C11})$$

as a solution, with $A^{\pm}(\tilde{t})$ an amplitude which varies slowly in time.

At $\mathcal{O}(\omega_{\text{on}})$, (C6) becomes

$$\Gamma \left(Y P_{u1}^{\pm} + P_{u1,Y}^{\pm} \right)_Y = P_{u0,\tilde{t}}^{\pm} + P_{u0}^{\pm}. \quad (\text{C12})$$

We highlight here the absence of the $\omega_0 e^{\gamma y} P_b^{\pm}$ term as we have assumed that $P_b^{\pm} \sim \omega_{\text{on}}$ in this region. Then (C12) may be integrated to

$$\Gamma \left[Y P_{u1}^{\pm} + P_{u1,Y}^{\pm} \right]_0^Y = \int_0^Y \left(A_{\tilde{t}}^{\pm} + A^{\pm} \right) e^{-\frac{1}{2}Y^2} dY \quad (\text{C13})$$

using the boundary conditions on flux (C7) at $Y = 0$. As the $Y P_{u1}^{\pm}$ term will dominate the left-hand side as $Y \rightarrow \infty$, we may write

$$\Gamma Y P_{u1}^{\pm} \approx \int_0^{\infty} \left(A_{\tilde{t}}^{\pm} + A^{\pm} \right) e^{-\frac{1}{2}Y^2} dY = \left(A_{\tilde{t}}^{\pm} + A^{\pm} \right) \sqrt{\frac{\pi}{2}}. \quad (\text{C14})$$

Then,

$$P_{u1}^{\pm} \approx \frac{1}{\Gamma Y} \left(A_{\tilde{t}}^{\pm} + A^{\pm} \right) \sqrt{\frac{\pi}{2}}, \quad (Y \gg 1). \quad (\text{C15})$$

Re-substitution of $Y = D_u^{-1/2} y$ gives

$$P_{u1}^{\pm} \approx \frac{1}{\Gamma y} \left(A_{\tilde{t}}^{\pm} + A^{\pm} \right) \sqrt{\frac{\pi D_u}{2}} \quad (\text{C16})$$

when $D_u^{1/2} \ll y$.

Now that we have an expression for how the shape of the unbound force generator pdf varies in time in region I, we seek similar solutions for the bound generator pdf in region III.

C.2 Region III

In region III we seek solutions of the form $P_b^\pm \sim P_{b0}^\pm + \omega_{\text{on}} P_{b1}^\pm + \dots$. Here, the pdf P_b^\pm is sharply peaked about $y_c = 1 \mp \tilde{z}_{\tilde{t}}$ over a diffusive length-scale $D_b^{1/2}$ (Figure 4h). Both $D_b^{1/2}$ and ω_{on} are assumed to be small parameters of similar order. Thus, in this region about the peak of P_b^\pm , we set $y = 1 \mp \tilde{z}_{\tilde{t}} + D_b^{1/2} \hat{Y}$. Noting that

$$\frac{\partial}{\partial \tilde{t}} \rightarrow \pm D_b^{-1/2} \tilde{z}_{\tilde{t}\tilde{t}} \frac{\partial}{\partial \hat{Y}} + \frac{\partial}{\partial \tilde{t}}, \quad \frac{\partial}{\partial y} \rightarrow D_b^{-1/2} \frac{\partial}{\partial \hat{Y}} \quad (\text{C17})$$

(C5b) becomes, to leading order,

$$\omega_{\text{on}} \left(P_{b,\tilde{t}}^\pm \pm D_b^{-1/2} \tilde{z}_{\tilde{t}\tilde{t}} P_{b,\hat{Y}}^\pm \right) - \left(D_b^{-1/2} v_b^\pm P_b^\pm + P_{b,\hat{Y}}^\pm \right)_{\hat{Y}} = \omega_{\text{on}} P_u^\pm - \omega_0 e^{\gamma(1 \mp \tilde{z}_{\tilde{t}})} P_b^\pm. \quad (\text{C18})$$

Recalling (8), (C18) may be further simplified to

$$\omega_{\text{on}} \left(P_{b,\tilde{t}}^\pm \pm D_b^{-1/2} \tilde{z}_{\tilde{t}\tilde{t}} P_{b,\hat{Y}}^\pm \right) - \left(\hat{Y} P_b^\pm + P_{b,\hat{Y}}^\pm \right)_{\hat{Y}} = \omega_{\text{on}} P_u^\pm - \omega_0 e^{\gamma(1 \mp \tilde{z}_{\tilde{t}})} P_b^\pm. \quad (\text{C19})$$

Substituting the expansion $P_b^\pm \approx P_{b0}^\pm + \omega_{\text{on}} P_{b1}^\pm + \dots$, to first order (C19) becomes

$$\left(\left(\hat{Y} \mp \omega_{\text{on}} D_b^{-1/2} \tilde{z}_{\tilde{t}\tilde{t}} \right) P_{b0}^\pm + P_{b0,\hat{Y}}^\pm \right)_{\hat{Y}} = 0 \quad (\text{C20})$$

taking $\omega_{\text{on}}/D_b^{1/2}$ to be $\mathcal{O}(1)$. By integration,

$$\left(Y \mp \omega_{\text{on}} D_b^{-1/2} \tilde{z}_{\tilde{t}\tilde{t}} \right) P_{b0}^\pm - P_{b0,Y}^\pm = C(\tilde{t}) \quad (\text{C21})$$

for $C(\tilde{t})$ some constant of integration. The boundary condition $J_b^\pm(\tilde{t}, y = y_{\text{max}}) = 0$ becomes $J_b^\pm(\tilde{t}, \hat{Y} \rightarrow \infty) \rightarrow 0$, while $J_b^\pm(\tilde{t}, y = 0) = 0$ becomes $J_b^\pm(\tilde{t}, \hat{Y} \rightarrow -\infty) \rightarrow 0$. Then

$$J_{b0}^\pm(\tilde{t}, \hat{Y} \rightarrow -\infty) + \omega_{\text{on}} J_{b1}^\pm(\tilde{t}, \hat{Y} \rightarrow -\infty) \rightarrow 0 \quad (\text{C22})$$

where

$$J_{b0}^\pm = D_b^{1/2} \left(\hat{Y} P_{b0}^\pm - P_{b0,\hat{Y}}^\pm \right), \quad (\text{C23a})$$

$$J_{b1}^\pm = D_b^{1/2} \left(\hat{Y} P_{b1}^\pm - P_{b1,\hat{Y}}^\pm \right) \quad (\text{C23b})$$

which must both separately also tend to zero as $\hat{Y} \rightarrow -\infty$. Using this, (C21) may be rewritten as

$$D_b^{-1/2} J_{b0}^\pm \mp \omega_{\text{on}} D_b^{-1/2} \tilde{z}_{\tilde{t}\tilde{t}} P_{b0}^\pm = C(\tilde{t}). \quad (\text{C24})$$

Making the assumption that $P_{b0}^\pm \rightarrow 0$ as $\hat{Y} \rightarrow -\infty$, which enforces (C22) at leading order, then $C(\tilde{t}) = 0$ and

$$P_{b0,\hat{Y}}^\pm = -\left(\hat{Y} \mp \omega_{\text{on}} D_b^{-1/2} \tilde{z}_{\tilde{t}\tilde{t}}\right) P_{b0}^\pm. \quad (\text{C25})$$

Integrating (C25) gives the solution

$$P_{b0}^\pm = \tilde{B}^\pm(\tilde{t}) e^{(-\frac{1}{2}\hat{Y}^2 \pm \omega_{\text{on}} D_b^{-1/2} \tilde{z}_{\tilde{t}\tilde{t}} \hat{Y})} = B^\pm(\tilde{t}) e^{(-\frac{1}{2}(\hat{Y} \mp \omega_{\text{on}} D_b^{-1/2} \tilde{z}_{\tilde{t}\tilde{t}})^2)} \quad (\text{C26})$$

for some $\tilde{B}^\pm(\tilde{t})$ and $B^\pm(\tilde{t})$, where $B^\pm(\tilde{t})$ describes the amplitude of the peak of the pdf (subject to smaller corrections) which varies in time. Returning to (C19), with $P_u^\pm \ll P_b^\pm$, then to $\mathcal{O}(\omega_{\text{on}})$

$$\left(\left(\hat{Y} \mp \omega_{\text{on}} D_b^{-1/2} \tilde{z}_{\tilde{t}\tilde{t}}\right) P_{b1}^\pm + P_{b1,\hat{Y}}^\pm\right)_{\hat{Y}} = P_{b0,\tilde{t}}^\pm + \frac{\omega_0 e^{\gamma(1 \mp \tilde{z}_{\tilde{t}})}}{\omega_{\text{on}}} P_{b0}^\pm, \quad (\text{C27})$$

which may be rewritten as

$$\left(D_b^{-1/2} J_{b1}^\pm \mp \omega_{\text{on}} D_b^{-1/2} \tilde{z}_{\tilde{t}\tilde{t}} P_{b1}^\pm\right)_{\hat{Y}} = P_{b0,\tilde{t}}^\pm + \frac{\omega_0 e^{\gamma(1 \mp \tilde{z}_{\tilde{t}})}}{\omega_{\text{on}}} P_{b0}^\pm. \quad (\text{C28})$$

Thus using (C26) in (C28) and integrating gives

$$\begin{aligned} \left[D_b^{-1/2} J_{b1}^\pm \mp \omega_{\text{on}} D_b^{-1/2} \tilde{z}_{\tilde{t}\tilde{t}} P_{b1}^\pm\right]_Y^\infty = \\ \int_Y^\infty \left(B_t^\pm \pm \omega_{\text{on}} D_b^{-1/2} \tilde{z}_{\tilde{t}\tilde{t}} \left(Y \mp \omega_{\text{on}} D_b^{-1/2} \tilde{z}_{\tilde{t}\tilde{t}}\right) B^\pm\right) e^{(-\frac{1}{2}(Y \mp \omega_{\text{on}} D_b^{-1/2} \tilde{z}_{\tilde{t}\tilde{t}})^2)} \\ + \left(\frac{\omega_0 e^{\gamma(1 \mp \tilde{z}_{\tilde{t}})}}{\omega_{\text{on}}} B^\pm\right) e^{(-\frac{1}{2}(Y \mp \omega_{\text{on}} D_b^{-1/2} \tilde{z}_{\tilde{t}\tilde{t}})^2)} dY. \end{aligned}$$

By assuming that $P_{b1}^\pm \rightarrow 0$ as $\hat{Y} \rightarrow \infty$, which enforces boundary condition $J_{b1}^\pm \rightarrow 0$ as $\hat{Y} \rightarrow \infty$, then

$$\begin{aligned} -D_b^{-1/2} J_{b1}^\pm \pm \omega_{\text{on}} D_b^{-1/2} \tilde{z}_{\tilde{t}\tilde{t}} P_{b1}^\pm = \\ \int_{\hat{Y}}^\infty \left(B_{\tilde{t}}^\pm \pm \omega_{\text{on}} D_b^{-1/2} \tilde{z}_{\tilde{t}\tilde{t}} \left(\hat{Y} \mp \omega_{\text{on}} D_b^{-1/2} \tilde{z}_{\tilde{t}\tilde{t}}\right) B^\pm\right) e^{(-\frac{1}{2}(\hat{Y} \mp \omega_{\text{on}} D_b^{-1/2} \tilde{z}_{\tilde{t}\tilde{t}})^2)} \\ + \left(\frac{\omega_0 e^{\gamma(1 \mp \tilde{z}_{\tilde{t}})}}{\omega_{\text{on}}} B^\pm\right) e^{(-\frac{1}{2}(\hat{Y} \mp \omega_{\text{on}} D_b^{-1/2} \tilde{z}_{\tilde{t}\tilde{t}})^2)} d\hat{Y}. \end{aligned}$$

The left-hand side (LHS) may be rewritten

$$\text{LHS} = -\left(\hat{Y} \mp D_b^{-1/2} \omega_{\text{on}} \tilde{z}_{\tilde{t}\tilde{t}}\right) P_{b1}^\pm + P_{b1,\hat{Y}}^\pm \quad (\text{C29})$$

and so in the limit $\hat{Y} \rightarrow -\infty$, (C29) is dominated by the $\hat{Y}P_{b1}^\pm$ term. Rearranging the right-hand side gives, in this limit,

$$\begin{aligned} -\hat{Y}P_{b1}^\pm &\sim \left(B_t^\pm + \frac{\omega_0 e^{\gamma(1 \mp \tilde{z}_t)}}{\omega_{\text{on}}} B^\pm \right) \int_{-\infty}^{\infty} e^{\left(-\frac{1}{2} (\hat{Y} \mp \omega_{\text{on}} D_b^{-1/2} \tilde{z}_{tt})^2 \right)} d\hat{Y} \\ &\quad \pm \omega_{\text{on}} D_b^{-1/2} \tilde{z}_{ttt} B^\pm \int_{-\infty}^{\infty} \left(\hat{Y} \mp \omega_{\text{on}} D_b^{-1/2} \tilde{z}_{tt} \right) e^{\left(-\frac{1}{2} (\hat{Y} \mp \omega_{\text{on}} D_b^{-1/2} \tilde{z}_{tt})^2 \right)} d\hat{Y}. \end{aligned}$$

The second integral vanishes, while the first integral can be evaluated and thus, as $\hat{Y} \rightarrow -\infty$,

$$P_{b1}^\pm \sim -\frac{\sqrt{2\pi}}{\hat{Y}} \left(B_t^\pm + \frac{\omega_0 e^{\gamma(1 \mp \tilde{z}_t)}}{\omega_{\text{on}}} B^\pm \right) = \frac{\sqrt{2\pi D_b}}{1 - y \mp \tilde{z}_t} \left(B_t^\pm + \frac{\omega_0 e^{\gamma(1 \mp \tilde{z}_t)}}{\omega_{\text{on}}} B^\pm \right). \quad (\text{C30})$$

The asymptotic limits (C16) and (C30) as $Y \rightarrow \infty$ and $\hat{Y} \rightarrow -\infty$ respectively will now be matched inside region II.

C.3 Region II

In region II, advection terms dominate. These ‘sweep’ the bound force generators toward the peak of P_b^\pm such that bound force generators will tend to have elastic linkers with an extension $y_c = 1 \mp \tilde{z}_t$, and the unbound force generators toward the peak of P_u^\pm such that unbound force generators will tend to have an elastic linker with zero extension. Given that the pdfs are peaked in regions I and II, $P_{b,y}^\pm$ and $P_{u,y}^\pm$ are both relatively small in region II, being given by the small correction terms $\omega_{\text{on}} P_{u1}^\pm$ and $\omega_{\text{on}} P_{b1}^\pm$, expressions for which we have determined in the limits $Y \rightarrow \infty$ and $\hat{Y} \rightarrow -\infty$ respectively. Then together, using (7a), $J_b^\pm = v_b^\pm P_b^\pm - D_b P_{b,y}^\pm \approx v_b^\pm P_b^\pm$, and so substitution of $P_b^\pm \approx \omega_{\text{on}} P_{b1}^\pm$ when $\hat{Y} \rightarrow -\infty$ and (8) returns

$$J_b^\pm \approx v_b^\pm P_b^\pm \approx \sqrt{2\pi D_b} \left(\omega_0 e^{\gamma(1 \mp \tilde{z}_t)} B^\pm + \omega_{\text{on}} B_t^\pm \right). \quad (\text{C31})$$

Continuing, using (7b), $J_u^\pm = -\Gamma (y P_u^\pm + D_u P_{u,y}^\pm) \approx -\Gamma y P_u^\pm$, and so substitution of $P_u^\pm \approx \omega_{\text{on}} P_{u1}^\pm$ when $Y \rightarrow \infty$ returns

$$J_u^\pm \approx -\Gamma y P_u^\pm \approx -\omega_{\text{on}} \sqrt{\frac{\pi D_u}{2}} (A^\pm + A_t^\pm). \quad (\text{C32})$$

By the form of (C31) and (C32), $J_{b,y}^\pm = 0$ and $J_{u,y}^\pm = 0$ to leading order, and therefore (C31) and (C32) are valid across the whole of region II. It follows that

$$J_b^\pm + J_u^\pm = \sqrt{D_u \omega_{\text{on}}} \left[\sqrt{\frac{2\pi D_b}{D_u}} \left(\frac{\omega_0}{\omega_{\text{on}}} e^{\gamma(1 \mp \tilde{z}_t)} B^\pm + B_t^\pm \right) - \sqrt{\frac{\pi}{2}} (A^\pm + A_t^\pm) \right] \quad (\text{C33})$$

is a constant across region II. As demonstrated in Online Resource 2(a,b), detailed balance ($J_b^\pm + J_u^\pm = 0$) does not hold in this region.

C.4 Matching solutions: Regions I-II

In region I it was assumed that P_b^\pm was sufficiently small ($\mathcal{O}(\omega_{\text{on}})$) that its dynamics could be neglected to leading order. By (C31) it can be estimated that P_b^\pm is of magnitude $\omega_{\text{on}}\sqrt{D_u}$, where it has been assumed that $D_b \sim D_u$. Then letting $P_b^\pm = \omega_{\text{on}}\sqrt{D_u}\hat{P}_b^\pm$ in (C5c) when $y = \sqrt{D_u}Y$ results in expressions for P_{u0}^\pm and P_{u1}^\pm which are unchanged from (C11) and (C16) respectively. However, (C5b) becomes

$$\omega_{\text{on}}\hat{P}_{b,t}^\pm + \frac{1}{\sqrt{D_u}} \left((1 \mp \tilde{z}_t - \sqrt{D_u}Y) \hat{P}_b^\pm - \sqrt{D_b}\hat{P}_{b,Y}^\pm \right)_Y = \frac{1}{\sqrt{D_u}} P_u^\pm - \omega_0 e^{\gamma\sqrt{D_u}Y} \hat{P}_b^\pm. \quad (\text{C34})$$

To leading order, (C34) becomes

$$(1 \mp \tilde{z}_t) \hat{P}_{b,Y}^\pm = P_{u0}^\pm = A^\pm e^{-Y^2/2}. \quad (\text{C35})$$

Then, integrating over Y from $Y = 0$ to $Y \rightarrow \infty$,

$$(1 \mp \tilde{z}_t) \hat{P}_b^\pm = \sqrt{\frac{\pi}{2}} A^\pm. \quad (\text{C36})$$

Assuming that $v_b^\pm \approx 1 \mp \tilde{z}_t$ to leading order, then

$$J_b^\pm \approx \omega_{\text{on}} \sqrt{\frac{D_u \pi}{2}} A^\pm. \quad (\text{C37})$$

Since J_b^\pm is independent of y in region II (Online Resource 2a,b), then we match (C31) to (C37), resulting in

$$\frac{\omega_0}{\omega_{\text{on}}} e^{\gamma(1 \mp \tilde{z}_t)} B^\pm + B_t^\pm = \frac{1}{2} \sqrt{\frac{D_u}{D_b}} A^\pm. \quad (\text{C38})$$

We now perform the same analysis on the boundary of regions II and III.

C.5 Matching solutions: Regions II-III

In region III it was assumed that P_u^\pm was sufficiently small that its dynamics could be neglected to leading order. By (C32) it can be estimated that P_u^\pm is of magnitude $\omega_{\text{on}}\sqrt{D_u}$. Then letting $P_u^\pm = \omega_{\text{on}}\sqrt{D_u}\hat{P}_u^\pm$ in (C5b) when $y = 1 \mp \tilde{z}_t + \sqrt{D_b}\hat{Y}$ results in expressions for P_{b0}^\pm and P_{b1}^\pm which are unchanged from (C26) and (C30) respectively. However, (C5c) becomes

$$\omega_{\text{on}} \left(\hat{P}_{u,t}^\pm \pm \frac{\tilde{z}_{tt}}{\sqrt{D_b}} \hat{P}_{u,\hat{Y}}^\pm \right) - \Gamma \left(\frac{1}{\sqrt{D_b}} (1 \mp \tilde{z}_t + \sqrt{D_b}\hat{Y}) \hat{P}_u^\pm + \frac{D_u}{D_b} \hat{P}_{u,\hat{Y}}^\pm \right)_{\hat{Y}}$$

$$= -\omega_{\text{on}} \hat{P}_{\text{u}}^{\pm} + \frac{\omega_0}{\omega_{\text{on}} \sqrt{D_{\text{u}}}} e^{\gamma(1 \mp \tilde{z}_i + \sqrt{D_{\text{b}}} \hat{Y})} P_{\text{b}}^{\pm}. \quad (\text{C39})$$

To leading order,

$$-\frac{\Gamma}{\sqrt{D_{\text{b}}}} (1 \mp \tilde{z}_i) \hat{P}_{\text{u}, \hat{Y}}^{\pm} = \frac{\omega_0}{\omega_{\text{on}} \sqrt{D_{\text{u}}}} e^{\gamma(1 \mp \tilde{z}_i)} P_{\text{b}0}^{\pm} = \frac{\omega_0}{\omega_{\text{on}} \sqrt{D_{\text{u}}}} e^{\gamma(1 \mp \tilde{z}_i)} B^{\pm} e^{-\frac{1}{2} (\hat{Y} \mp \omega_{\text{on}} D_{\text{b}}^{-1/2} \tilde{z}_{i\bar{i}})^2} \quad (\text{C40})$$

where we have used that $e^{\gamma(1 \mp \tilde{z}_i + \sqrt{D_{\text{b}}} \hat{Y})} = e^{\gamma(1 \mp \tilde{z}_i)} e^{\gamma \sqrt{D_{\text{b}}} \hat{Y}} \approx e^{\gamma(1 \mp \tilde{z}_i)}$ as $\sqrt{D_{\text{b}}}$ is a small parameter. Integrating from $\hat{Y} \rightarrow -\infty$ to $\hat{Y} \rightarrow \infty$ gives

$$\Gamma (1 \mp \tilde{z}_i) \hat{P}_{\text{u}}^{\pm} = \sqrt{\frac{D_{\text{b}}}{D_{\text{u}}}} \frac{\omega_0}{\omega_{\text{on}}} e^{\gamma(1 \mp \tilde{z}_i)} B^{\pm} \sqrt{2\pi}. \quad (\text{C41})$$

Taking $y \approx 1 \mp \tilde{z}_i$ to leading order, then

$$J_{\text{u}}^{\pm} \approx -\sqrt{2\pi D_{\text{b}}} \omega_0 e^{\gamma(1 \mp \tilde{z}_i)} B^{\pm}. \quad (\text{C42})$$

Since J_{u}^{\pm} is independent of y in region II (Online Resource 2a,b), then we match (C32) to (C42) resulting in

$$\frac{\omega_0}{\omega_{\text{on}}} e^{\gamma(1 \mp \tilde{z}_i)} B^{\pm} = \frac{1}{2} \sqrt{\frac{D_{\text{u}}}{D_{\text{b}}}} (A^{\pm} + A_{\bar{i}}^{\pm}). \quad (\text{C43})$$

C.6 Combining the whole system

We may now use expressions (C11), (C16) for P_{b}^{\pm} and (C26), (C30) for P_{u}^{\pm} , and their coupling in region II (C38, C43) to close the system. Recalling (12), then to leading order

$$\int_0^{\infty} \left(A^{\pm} e^{-\frac{1}{2D_{\text{u}}} y^2} + B^{\pm} e^{-\frac{1}{2D_{\text{b}}} (y - 1 \pm \tilde{z}_i \mp \omega_{\text{on}} \tilde{z}_{i\bar{i}})^2} \right) dy = 1. \quad (\text{C44})$$

The first term of this integral is easily evaluated, while the second term is more complex. Consider only the leading-order terms of the exponent, due to ω_{on} being a small order parameter. Then

$$\int_0^{\infty} B^{\pm} e^{-\frac{1}{2D_{\text{b}}} (y - 1 \pm \tilde{z}_i \mp \omega_{\text{on}} \tilde{z}_{i\bar{i}})^2} dy \approx \int_0^{\infty} B^{\pm} e^{-\frac{1}{2D_{\text{b}}} (y - y_c)^2} dy \quad (\text{C45})$$

which we know is a peak contained within region III. That is, we integrate over the Gaussian, which does not intersect $y = 0$ with any value of significance at leading order. Using this logic, the integral (C45) may be evaluated and thus

$$A^{\pm} \sqrt{\frac{\pi D_{\text{u}}}{2}} + B^{\pm} \sqrt{2\pi D_{\text{b}}} = 1. \quad (\text{C46})$$

This can be used to eliminate A^\pm from (C38) to give

$$\sqrt{2\pi D_b} B_t^\pm = 1 - \sqrt{2\pi D_b} \left(\frac{\omega_0}{\omega_{\text{on}}} e^{\gamma(1 \mp \tilde{z}_t)} + 1 \right) B^\pm. \quad (\text{C47})$$

(C46) may similarly be used in (C43) to return (C47).

Equation (C47) predicts that $\sqrt{2\pi D_b} B^\pm$ relaxes to $\omega_{\text{on}}/\{\omega_{\text{on}} + \omega_0 e^{\gamma(1 \mp \tilde{z}_t)}\}$ and (C46) predicts that $\sqrt{\pi D_u/2} A^\pm$ relaxes to $\omega_0 e^{\gamma(1 \mp \tilde{z}_t)}/\{\omega_{\text{on}} + \omega_0 e^{\gamma(1 \mp \tilde{z}_t)}\}$ provided \tilde{z} does not change too rapidly.

Further to this, $P_b^\pm = P_{b0}^\pm + \omega_{\text{on}} P_{b1}^\pm + \dots$ can be put into (C5a) to obtain a leading-order equation for the motion of the spindle pole. This requires the evaluation of

$$\int_0^{y_{\text{max}}} y P_b^\pm dy \sim \int_0^\infty y B^\pm e^{\left(-\frac{1}{2D_b}(y-y_c)\right)^2} dy + \dots \quad (\text{C48})$$

where we assume y_{max} is sufficiently large that it exceeds the bounds of region III and can thus be taken as $y_{\text{max}} \rightarrow \infty$. Again we let $y = y_c + D_b^{1/2} \hat{Y}$, which is where P_{b0}^\pm has a significant value. Then

$$\int_0^\infty y B^\pm e^{\left(-\frac{1}{2D_b}(y-y_c)\right)^2} dy \sim \int_{-\infty}^\infty \left(y_c + D_b^{1/2} \hat{Y}\right) B^\pm e^{-\frac{1}{2} \hat{Y}^2} D_b^{1/2} d\hat{Y}, \quad (\text{C49})$$

which to leading order becomes

$$\begin{aligned} \int_{-\infty}^\infty \left(y_c + D_b^{1/2} \hat{Y}\right) B^\pm e^{-\frac{1}{2} \hat{Y}^2} D_b^{1/2} d\hat{Y} &\sim D_b^{1/2} y_c B^\pm \int_{-\infty}^\infty e^{-\frac{1}{2} \hat{Y}^2} d\hat{Y} \\ &= y_c B^\pm \sqrt{2\pi D_b} + \dots \end{aligned} \quad (\text{C50})$$

Recalling that $y_c = 1 \mp \tilde{z}_t$, (C5a) becomes

$$\xi \tilde{z}_t = -\frac{K}{\omega_{\text{on}}} \tilde{z} - N \sqrt{2\pi D_b} \left((1 + \tilde{z}_t) B^- - (1 - \tilde{z}_t) B^+ \right) \quad (\text{C51})$$

and thus

$$\xi \tilde{z}_t = -\frac{K}{\omega_{\text{on}}} \tilde{z} - N \sqrt{2\pi D_b} (B^- + B^+) \tilde{z}_t - N \sqrt{2\pi D_b} (B^- - B^+). \quad (\text{C52})$$

This can be rewritten as

$$\left(\hat{\xi} + \hat{B}^+ + \hat{B}^- \right) \tilde{z}_t + \hat{K} \tilde{z} = \hat{B}^+ - \hat{B}^-, \quad (\text{C53})$$

where $\hat{B}^\pm = \sqrt{2\pi D_b} B^\pm$, $\hat{K} = K/\{\omega_{\text{on}} N\}$, and $\hat{\xi} = \xi/N$. Recalling (C47) which may be alternatively written as

$$\left(1 + \rho e^{\gamma(1 \mp \tilde{z}_t)} \right) \hat{B}_t^\pm + \hat{B}_t^\pm = 1 \quad (\text{C54})$$

where $\rho = \omega_0/\omega_{\text{on}}$, the coupled system (7a), (7b), and (10) is reduced to solving (C53, C54) along with initial conditions on \tilde{z}_0 and \hat{B}_0^\pm .

References

- Belyy V, Hendel NL, Chien A, et al (2014) Cytoplasmic dynein transports cargos via load-sharing between the heads. *Nature Comm* 5(1):1–9
- Bergstrahl DT, St Johnston D (2014) Spindle orientation: what if it goes wrong? In: *Seminars Cell Dev. Biol.*, Elsevier, pp 140–145
- Bosveld F, Markova O, Guirao B, et al (2016) Epithelial tricellular junctions act as interphase cell shape sensors to orient mitosis. *Nature* 530(7591):495–498
- Burakov A, Nadezhdina E, Slepchenko B, et al (2003) Centrosome positioning in interphase cells. *J Cell Biol* 162(6):963–969
- Compton DA, Cleveland DW (1993) NuMA is required for the proper completion of mitosis. *J Cell Biol* 120(4):947–957
- Corrigan AM, Shrestha R, Draviam VM, et al (2015) Modeling of noisy spindle dynamics reveals separable contributions to achieving correct orientation. *Biophys J* 109(7):1398–1409
- Dogterom M, Kerssemakers JW, Romet-Lemonne G, et al (2005) Force generation by dynamic microtubules. *Curr Op Cell Biol* 17:67–74
- Erban R, Chapman SJ (2020) *Stochastic modelling of reaction–diffusion processes*, vol 60. Cambridge University Press
- Ezber Y, Belyy V, Can S, et al (2020) Dynein harnesses active fluctuations of microtubules for faster movement. *Nature Physics* 16(3):312–316
- Gillespie DT (1977) Exact stochastic simulation of coupled chemical reactions. *J Phys Chem* 81(25):2340–2361
- Goddard GK, Tarannum N, Woolner S (2020) Applying tensile and compressive force to xenopus animal cap tissue. *Cold Spring Harbor Protocols* 2020(3):pdb–prot105551
- Grill S, Kruse K, Jülicher F (2005) Theory of mitotic spindle oscillations. *Phys Rev Lett* 94(10):108104
- Harborth J, Weber K, Osborn M (1995) Epitope mapping and direct visualization of the parallel, in-register arrangement of the double-stranded coiled-coil in the NuMA protein. *EMBO J* 14(11):2447–2460

- Hargreaves D (2023) Mitotic spindle dynamics in stretched epithelial tissue *in vivo* and *in silico*. PhD thesis, University of Manchester, UK
- Howard J (2006) Elastic and damping forces generated by confined arrays of dynamic microtubules. *Phys Biol* 3(1):54–66
- Joshi SD, Davidson LA (2010) Live-cell imaging and quantitative analysis of embryonic epithelial cells in *xenopus laevis*. *JoVE (Journal of Visualized Experiments)* (39):e1949
- Karsenti E, Vernos I (2001) The mitotic spindle: a self-made machine. *Science* 294(5542):543–547
- Larson ME, Bement WM (2017) Automated mitotic spindle tracking suggests a link between spindle dynamics, spindle orientation, and anaphase onset in epithelial cells. *Mol Biol Cell* 28(6):746–759
- Li J, Jiang H (2017) Geometric asymmetry induces upper limit of mitotic spindle size. *Biophys J* 112(7):1503–1516
- Li J, Cheng L, Jiang H (2019) Cell shape and intercellular adhesion regulate mitotic spindle orientation. *Mol Biol Cell* 30(19):2458–2468
- Milo R, Phillips R (2015) Cell biology by the numbers. Garland Science
- Minc N, Burgess D, Chang F (2011) Influence of cell geometry on division-plane positioning. *Cell* 144(3):414–426
- Mitchison T, Salmon E (2001) Mitosis: a history of division. *Nature Cell Biol* 3(1):E17–E21
- Morin X, Bellaïche Y (2011) Mitotic spindle orientation in asymmetric and symmetric cell divisions during animal development. *Dev Cell* 21(1):102–119
- Nestor-Bergmann A, Goddard G, Woolner S, et al (2018) Relating cell shape and mechanical stress in a spatially disordered epithelium using a vertex-based model. *Math Med Biol* 35(Supplement_1):i1–i27
- Nestor-Bergmann A, Stooke-Vaughan GA, Goddard GK, et al (2019) Decoupling the roles of cell shape and mechanical stress in orienting and cueing epithelial mitosis. *Cell reports* 26(8):2088–2100
- Okumura M, Natsume T, Kanemaki MT, et al (2018) Dynein–dynactin–NuMA clusters generate cortical spindle-pulling forces as a multi-arm ensemble. *Elife* 7:e36559
- Pecreaux J, Röper JC, Kruse K, et al (2006) Spindle oscillations during asymmetric cell division require a threshold number of active cortical force generators. *Curr Biol*

16(21):2111–2122

- Pecreaux J, Redemann S, Alayan Z, et al (2016) The mitotic spindle in the one-cell *C. elegans* embryo is positioned with high precision and stability. *Biophys J* 111(8):1773–1784
- Phillips NE, Manning CS, Pettini T, et al (2016) Stochasticity in the mir-9/hes1 oscillatory network can account for clonal heterogeneity in the timing of differentiation. *Elife* 5:e16118
- Rubinstein B, Larripa K, Sommi P, et al (2009) The elasticity of motor–microtubule bundles and shape of the mitotic spindle. *Phys Biol* 6(1):016005
- Schneider CA, Rasband WS, Eliceiri KW (2012) Nih image to imagej: 25 years of image analysis. *Nature methods* 9(7):671–675
- Tang Z, Hu Y, Wang Z, et al (2018) Mechanical forces program the orientation of cell division during airway tube morphogenesis. *Dev Cell* 44(3):313–325
- Théry M, Jiménez-Dalmaroni A, Racine V, et al (2007) Experimental and theoretical study of mitotic spindle orientation. *Nature* 447(7143):493–496
- Troster M, Mücke N, Surrey T (2012) Reconstitution of the human cytoplasmic dynein complex. *Proc Nat Acad Sci* 109(51):20895–20900
- Tsimring LS (2014) Noise in biology. *Rep Prog Phys* 77(2):026601
- Woolner S, Miller AL, Bement WM (2010) Imaging the cytoskeleton in live xenopus laevis embryos. *Cytoskeleton Meth Protocols* pp 23–39
- Zhu J, Burakov A, Rodionov V, et al (2010) Finding the cell center by a balance of dynein and myosin pulling and microtubule pushing: a computational study. *Mol Biol Cell* 21(24):4418–4427